AN ABSTRACT OF THE THESIS OF

Susan P. Klein for the degree of Doctor of Philosophy in Physics presented on October 25, 1995. Title: Nuclear Magnetic Resonance and Nuclear Quadrupole Resonance Study of Atomic Motion in $YBa_2Cu_3O_7$.

Abstract approved: Redacted for Privacy

William W. Warren, Jr.

The evolution of the ^{63}Cu nuclear quadrupole resonance (NQR) and nuclear magnetic resonance (NMR) spectra over a temperature range from -100°C to 200°C was studied in samples close to the composition $YBa_2Cu_3O_7$. For both the Cu(1) and Cu(2) sites there is an unexpected loss of signal intensity at higher temperatures. The onset of this loss occurs at higher temperatures in samples of higher quality as indicated by their room temperature NQR spectra. This loss was determined to be caused by an extra component to the transverse relaxation. The results are interpreted in terms of the effect that oxygen motion in the chain layer would have on the NQR and NMR spin echoes. The jump rate showed an activation energy of 0.64 eV and an attempt frequency of 10^{11} s^{-1} for the higher quality sample. The lower quality sample showed a thermal activation energy of 0.2 eV and an attempt frequency of 10^6 s^{-1}. The difference in attempt frequencies and activation energies is discussed in terms of terms of a transition from individual to correlated oxygen jumps in the chain layer.

Nuclear Magnetic Resonance and Nuclear Quadrupole Resonance Study of Atomic Motion in $YBa_2Cu_3O_7$

by

Susan P. Klein

A DISSERTATION

submitted to

Oregon State University

in partial fulfillment of
the requirements for the
degree of

Doctor of Philosophy

Completed October 25, 1995
Commencement June 1996

Doctor of Philosophy dissertation of Susan P. Klein presented on October 25, 1995

APPROVED:

Redacted for Privacy

Major Professor, representing Physics

Redacted for Privacy

Chair of Department of Physics

Redacted for Privacy

Dean of Graduate School

I understand that my dissertation will become part of the permanent collection of Oregon State University libraries. My signature below authorizes release of my dissertation to any reader upon request.

Redacted for Privacy

Susan P. Klein, Author

ACKNOWLEDGEMENT

I would like to acknowledge Dr. Arthur Sleight, Dr. Rui-Ping Wang, and Matt Hall for providing the samples that were used in my study. I am indebted to both Dr. Sleight and Dr. John Gardner for their contributions during several discussions concerning my project. I am grateful to Show-Jye Cheng, a fellow graduate student in Dr. Warren's research group, who instructed me on the CMX spectrometer.

Of course many people have helped me along the path to my Ph. D. My thanks go out to my hometown teachers who set me on the path. My love and thanks go to all the family and friends who cheered me on and lent me emotional support when I needed it.

The biggest thanks of all goes to my advisor, Dr. William Warren. This dissertation would never have been possible without his time, advice, discussions, and humor.

DEDICATION

This thesis is dedicated to my grandparents, William and Vera Klein, who planned for my education from the beginning.

TABLE OF CONTENTS

TABLE OF CONTENTS (Continued)

LIST OF FIGURES

LIST OF FIGURES (Continued)

LIST OF FIGURES (Continued)

LIST OF TABLES

NUCLEAR MAGNETIC RESONANCE AND NUCLEAR QUADRUPOLE RESONANCE STUDY OF ATOMIC MOTION IN $YBa_2Cu_3O_7$

1. INTRODUCTION

The compound $YBa_2Cu_3O_{6+x}$ is a high-temperature, type II superconductor whose electrical resistance becomes zero below a critical temperature, T_c. Although it is one of the most widely studied type II superconductors, much is still not understood about it and the mechanism of type II superconductivity.

Nuclear magnetic resonance (NMR) and nuclear quadrupolar resonance (NQR) act as local probes of an atom's environment, providing information on the microscopic structure of the material being studied. Because of their sensitivity to the electromagnetic environment, both have been used to study high-temperature superconductivity and $YBa_2Cu_3O_{6+x}$.

1.1 $YBa_2Cu_3O_{6+x}$

1.1.1 Structure

$YBa_2Cu_3O_{6+x}$ has a perovskite related structure. Like many other high-temperature superconductors, it made up of Cu-O layers. (See Fig. 1.1) The Cu(1) and O(1) sites make up the chain layer, with the oxygens lined up in chains along the b-direction. The O(5) sites are in the a-direction and are unoccupied as a general rule. (See

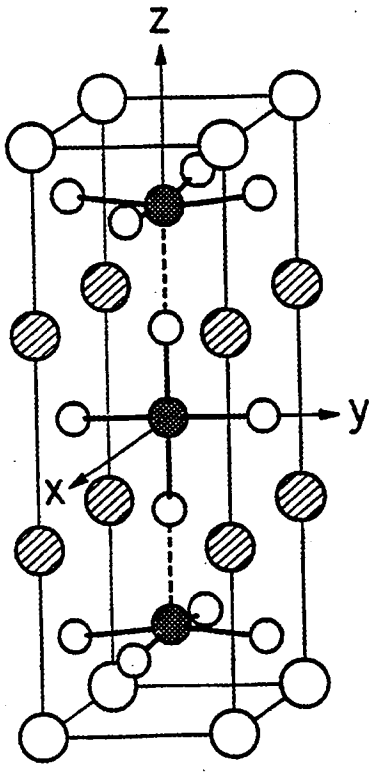

Figure 1.1. $YBa_2Cu_3O_7$ unit cell. Solid circles are Cu atoms, shaded circles denote Ba, small open circles are oxygen, and large open circles at cell corners denote Y atoms. From ref. (1).

Fig. 1.2) They are sometimes referred to as the interstitial sites. Most oxygen vacancies are located at the O(1) sites. The diffusion of oxygen usually takes place in the chain layer. (See Sec. 3.2.4) The Cu(2), O(2), and O(3) sites make up the plane layer, with two plane layers per unit cell. The O(2) sites lie in the a-direction, and the O(3) sites are in the b-direction. These oxygen sites are usually fully occupied. It is believed that the carriers for superconductivity are located in these planes. The O(4) site, or the apical oxygen, links the chain and plane layers.

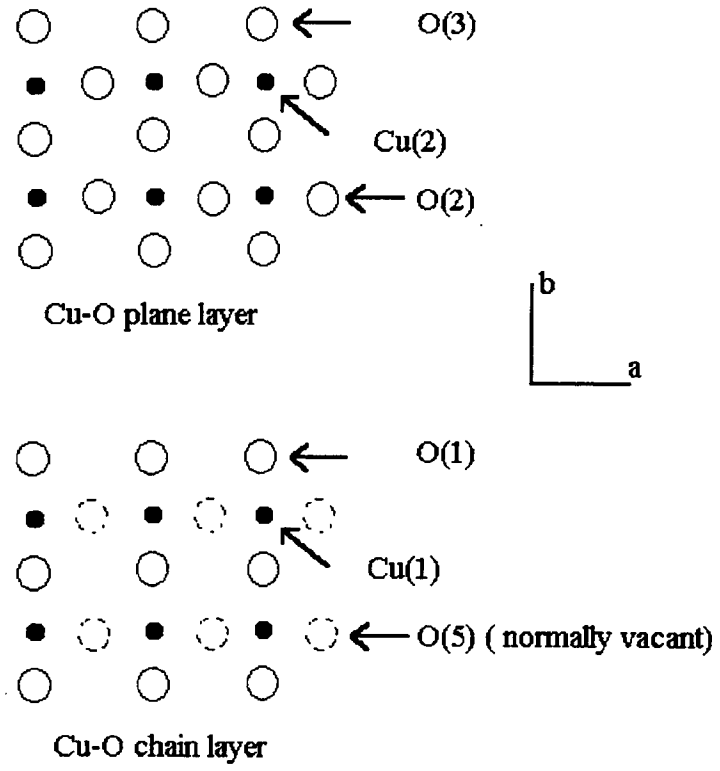

Figure 1.2. Structure and labeling of the Cu-O layers.

The structure of $YBa_2Cu_3O_{6+x}$ is partially determined by its oxygen content. The oxygen content varies from six to seven oxygens per unit cell. Usually, a sample is described as being O_6, $O_{6.5}$, etc., with the subscript referring to the average number of oxygen atoms per unit cell. The two standards for labeling the oxygen content are $YBa_2Cu_3O_{7-\delta}$ and $YBa_2Cu_3O_{6+x}$. In the ideal structure the material is fully oxygenated, or O_7. All of the O(1) sites are filled, creating an orthorhombic structure in which the a-axis is shorter than the b-axis. A second orthorhombic structure occurs for the $O_{6.5}$ material, in which half of the oxygens are missing from the chain sites. The oxygen atoms order into

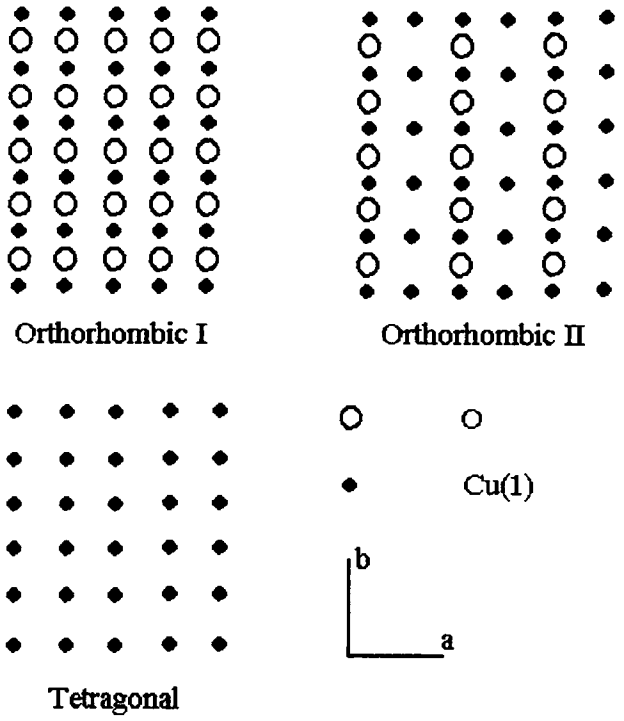

Figure 1.3. Ordered structures of the Cu-O chain layer.

an alternating full and empty chain structure. (See Fig. 1.3) The structure for the fully oxygenated material is labeled orthorhombic I. The alternating full and empty chains structure is labeled orthorhombic II. The final structure is tetragonal, $O_{6.0}$, with no oxygen in the chain sites. The a and b directions are equivalent. While the othorhombic structure is superconducting, the tetragonal structure is not.[1,2,3]

There are also subtle structural differences that depend upon the oxygen content. The plane layer is actually buckled for the fully oxygenated material, with the O(2) and O(3) oxygens being displaced away from the chain layer with respect to the Cu(2) site. (See Fig. 1.4) As the oxygen is removed the two oxygen sites will become equivalent, and

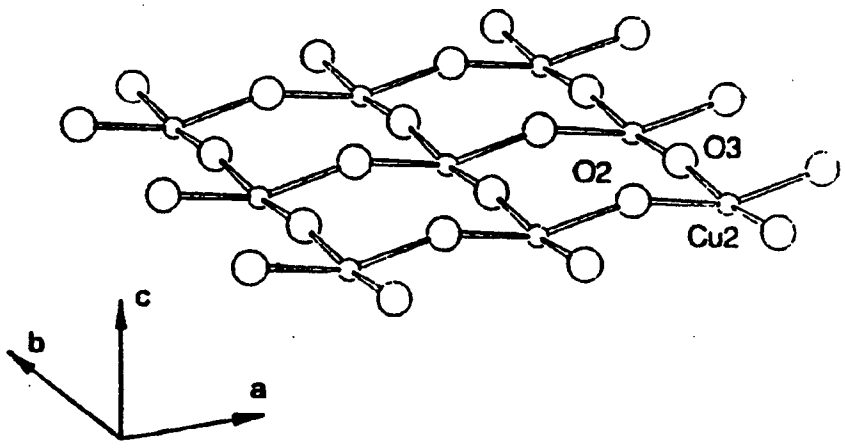

Figure 1.4. Buckled structure of the Cu-O plane. From ref. (5).

the buckling will decrease. It is thought that the coherent buckling of this layer may be related to superconductivity.[4]

1.1.2 Superconductivity and Oxygen Content

$YBa_2Cu_3O_{6+x}$ behaves as a high-temperature superconductor for oxygen contents above $O_{6.35}$. The critical temperature is dependent upon the oxygen content, with the O_7 material having the highest critical temperature at 93K. (See Fig. 1.5) The superconductivity is possible due to the presence of hole carriers. In the O_7 material, the the formal valence would be +2e on the Cu(2) atom and +3e on the Cu(1) atom by charge conservation. In actuality, the Cu(1) site has a charge close to +2e. The remaining positive charge, or hole, is free to become a hole carrier in the Cu(2) planes. As the

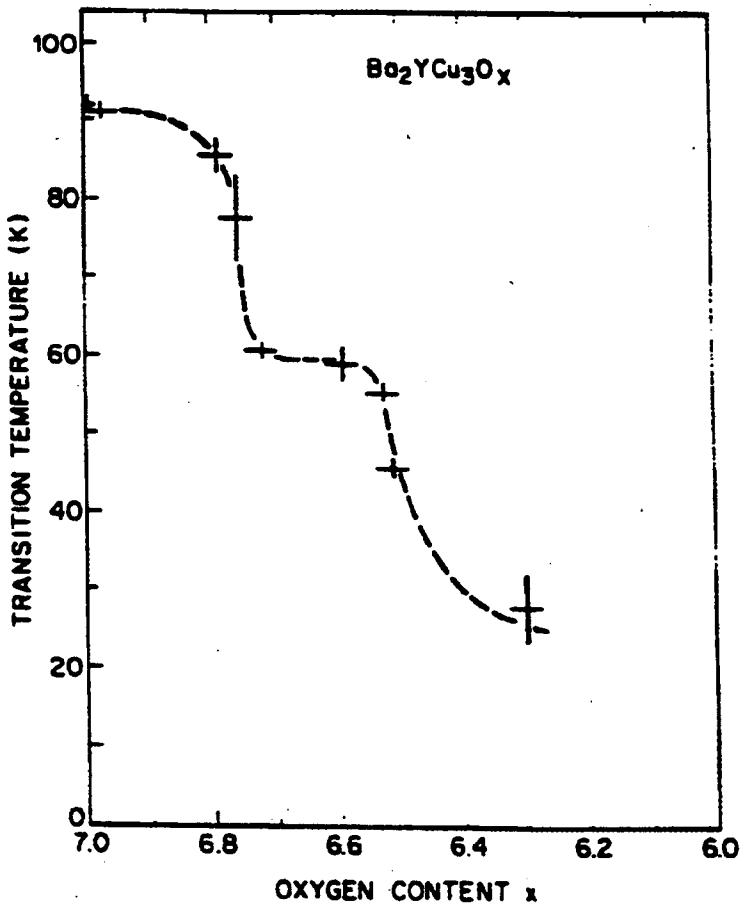

Figure 1.5. T_c dependence on oxygen content. From ref. (6).[5]

oxygen content is decreased, the average expected charge on the Cu(1) atom is decreased, which decreases the positive charges available to become carriers.

1.2 Motivation and Outline of Project

Using NMR and NQR to study $YBa_2Cu_3O_{6+x}$, Dr. William W. Warren, Jr. noticed that above room temperature, the NQR signal became unobservable at a lower than

expected temperature. Preliminary studies done by myself confirmed that this was indeed the case, and that the signal intensity did not obey the Curie Law above a certain temperature. (See Sec. 2.3.1) A review of the literature suggested oxygen motion as a possible candidate for the cause of this effect. The motion of oxygen is of interest because the diffusion and ordering of the oxygen atoms at higher temperatures determines the properties of the material at lower temperatures. There have been a number of experiments pertaining to oxygen motion, but the majority examine the bulk diffusion of oxygen, not the short range motion of the oxygen atoms.

This project studies $YBa_2Cu_3O_{6+x}$'s unexpected loss of intensity of the NQR signal near room temperature using NQR and NMR. The effect that elevated temperatures have on different samples will be examined. The spin-spin relaxation rates will also be examined for different samples and temperatures.

2. BASIC CONCEPTS OF NUCLEAR MAGNETIC RESONANCE[6,7]

2.1 The Quantum Mechanical Basis of NMR

Every nucleus has a value $\vec{I}$ associated with it which corresponds to its angular momentum. If the magnitude of this vector is measured, the values found for I are quantized in integer or half integer values. Any nucleus with an I greater than zero has a magnetic dipole moment which may be detected by using nuclear magnetic resonance. Nuclear quadrupole resonance requires $I \geq 1$. When the projection of $\vec{I}$ onto the z-axis is measured, it is found that I_z has 2I+1 eigenstates which may be denoted by m. The eigenstate m may have values m = -I, -I+1, ..., I-1, I.

The nucleus has a magnetic moment $\vec{\mu} = \gamma\hbar\vec{I}$, where γ is the gyromagnetic ratio. The value of the gyromagnetic ratio varies for different nuclear isotopes and may be found in tables. The energies associated with the eigenstates m are degenerate in the absence of external fields. In nuclear magnetic resonance (NMR) the degeneracy is lifted by applying a magnetic field $\vec{H}_0$. This creates energy levels $E = -\vec{\mu}\cdot\vec{H}_0 = -\gamma\hbar\vec{I}\cdot\vec{H}_0$. If $\vec{H}_0$ is in the z-direction, the values are quantized yielding $E_m = -\gamma\hbar H_0 m$. (See Fig. 2.1) The energy levels are equally separated. Assuming a one-photon magnetic dipole process for transitions between these levels, the selection rules require $\Delta m = \pm 1$, which leads to $\Delta E = -\gamma\hbar\vec{H}_0$. The energy required to cause a transition between energy levels may be created by a time-dependent electromagnetic field of frequency $\omega_0 = \gamma H_0$. For typical laboratory magnetic fields, frequencies are in the megahertz, or radio frequency (RF), range.

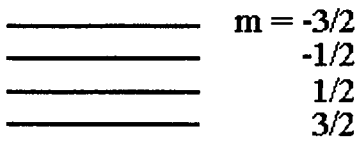

Figure 2.1. Energy levels for I = 3/2.

2.2 Classical Model for Magnetic Dipole

A classical approach to understanding how the nucleus responds to external electromagnetic fields is helpful. The magnetic moment of the nucleus experiences a torque from the magnetic field. As the nucleus has an angular momentum, its behavior is very similar to that of a gyroscope. Classically, $\vec{\tau} = d\vec{I} / dt$ and $\vec{\tau} = \vec{\mu} \times \vec{H}_0$. Assuming $\vec{H}_0$ is in the z-direction, the torque causes the nucleus to precess around the z-axis at an angle θ from the z-axis and with a frequency ω_L, which is known as the Larmor frequency. This frequency is the same as the frequency ω_0 that was found earlier. For multiple nuclei, the phases of the individual nuclei differ causing the x and y components of the macroscopic magnetization to add up to zero. However, there is an overall macroscopic magnetization in the z-direction as the spins partially align with the magnetic field.

For the next step, it is easiest to switch reference frames from the static lab frame to a rotating frame. The rotating frame has the same z-axis as the lab frame but is rotating at the frequency ω_0. Now $\vec{H}_1$, a second field much smaller than and perpendicular to the first, is applied to the nucleus. If $\vec{H}_1$ has a frequency ω_0, it will then appear static in the rotating frame. Now the nucleus can again be treated as a spin in a static field. It will now

precess in the rotating frame around the axis of $\vec{H}_1$ at a frequency $\omega = \gamma H_1$. This will cause changes to θ and the potential energy of the nucleus in the magnetic field, which are analogous to the transitions between the energy levels of different m. The angle of the magnetization, θ, is given by ωt. By controlling the time that $\vec{H}_1$ is applied, the direction of the magnetization can be controlled. For example, to invert the magnetization, $\vec{M}$, $\theta = \pi$. To bring $\vec{M}$ into the x-y plane, $\theta = \pi / 2$.

In an NMR experiment, $M_x(t)$ is measured. Using a coil with its axis perpendicular to $\vec{H}_0$, $M_x(t)$ may be detected by the currents induced by the time dependent magnetization.

2.3 Thermal Equilibrium

The thermal equilibrium of the spins has several consequences. The most important consequence for my project is the Curie law of magnetic susceptibility, which describes the relationship between the magnetization and the temperature. Another consequence is the net magnetization's return to thermal equilibrium after a perturbation of the Zeeman energy levels' populations by spin-lattice relaxation.

2.3.1 Curie Law

At thermal equilibrium, the populations of the energy levels can be described by the Boltzmann distribution $N(E) = N_0 \exp(-E / kT)$. For a system of N spins in a

magnetic field, the population of each sublevel m will be

$$N(m) = \frac{N}{2I+1}\exp\left(\frac{m\gamma\hbar H_0}{kT}\right). \qquad \text{(Eqn. 2.1)}$$

The net magnetization is then

$$M = N\gamma\hbar\frac{\sum_{m=-I}^{I} m\exp(\gamma\hbar m H_0 / kT)}{\sum_{m=-I}^{I}\exp(\gamma\hbar H_0 / kT)}. \qquad \text{(Eqn. 2.2)}$$

Assuming $m\gamma\hbar H_0 / kT$ is very small, an expansion may be made which yields

$$M = \frac{N\gamma^2\hbar^2 I((I+1)H_0}{3kT}. \qquad \text{(Eqn. 2.3)}$$

For a constant field, $MT = C$, where $C = N\gamma^2\hbar^2 I(I+1)/3kT$ is the Curie Constant. This relationship is known as the Curie law.

2.3.2 Spin-Lattice Relaxation Rate T_1

When the field $\vec{H}_1$ is removed from the spin system, the spins will return to precessing around $\vec{H}_0$. The process involved in the relaxation of the net magnetization back to the z-axis requires an exchange of energy between the spins and the lattice, hence the name spin-lattice relaxation. Because it involves a relaxation of the net magnetization along the z-axis, it is sometimes referred to as the longitudinal relaxation.

The behavior of the net magnetization as it relaxes is often described by the use of phenomenological Bloch equations. The rate of change of M will depend on the rate of the transitions into the various states. An example for a two level system would be

$$\frac{1}{T_1} = W_{\downarrow} + W_{\uparrow}, \qquad \text{(Eqn. 2.5)}$$

where W represents the rate of transition into a particular state. The Bloch equation describing this behavior is

$$\frac{dM_z}{dt} = \frac{M_0 - M_z}{T_1}, \qquad \text{(Eqn. 2.6)}$$

where M_0 is the equilibrium magnetization. Integrating this yields

$$M_z(t) = M_0\left(1 - \exp\left(-t / T_1\right)\right). \qquad \text{(Eqn. 2.7)}$$

Once $\vec{H}_1$ is removed, the system will approach thermal equilibrium exponentially with a time constant T_1.

2.4 Spin-Spin Relaxation Rate T_2

The transverse magnetization, M_x and M_y, will decay to zero when the applied field, $\vec{H}_1$, is removed. This decay is known as spin-spin or transverse relaxation and may have several processes causing it. The time T_2 is a measure of how long the individual spins which create the net transverse magnetization remain in phase with each other. One cause of the dephasing of the spins is differences in the local magnetic field that each spin sees, which causes each one to precess at a slightly different angular velocity. Another cause is changing local fields. (See Sec. 4.3.1) T_2 is always smaller than T_1.

2.5 Hyperfine Interactions

Up to this point, I have only discussed the interactions that are universal for all nuclei that are used in NMR. In most materials, there are also internal interactions that can perturb the Zeeman energy levels or lead to relaxation processes. Some examples of such interactions are electric quadrupole interactions, contact hyperfine interactions, and the orbital angular momentum of the electrons.

2.5.1 Knight Shift and Chemical Shift

Some interactions can raise or lower the effective magnetic field. Typically, this is handled by replacing H_0 with $H_0 + H'$. An example of this is the Knight shift, which is caused by a contact hyperfine interaction by which the conduction electrons in the s-orbital couple to the nucleus. The Knight shift is usually given as a percent shift, typically on the order of 0.1 to 1.0%, of the Larmor frequency and almost always increases the effective field. Another example is the chemical shift which usually lowers the effective magnetic field seen by the nucleus. It is caused by the orbital angular momentum of the electrons shielding the nucleus from the external magnetic field. Chemical shift data are usually given as the difference between the experimental sample's and a reference samples' frequency in parts per million.

2.5.2 Quadrupolar Interactions

Previously, I discussed the Zeeman interaction for a magnetic dipole. However, any nucleus with $I \geq 1$ has an electric quadrupole moment due to the distribution of charge within the nucleus. For spin 3/2, the nucleus has an electric-quadrupole which will perturb the Zeeman levels. (See Fig. 2.2) If the nucleus is placed in a charge distribution created by the fixed lattice charges which has a lower than cubic symmetry, it will demonstrate a preferred alignment which is present even in the absence of an external magnetic field. This is the basis for quadrupolar perturbed NMR and nuclear quadrupole resonance (NQR).

The electric field gradient is defined by the matrix $V_{ij} = \partial V/\partial x_i\, \partial x_j$. In the principal axis frame, this matrix is diagonalized and the condition $\nabla^2 V = 0$ is satisfied. This permits the field gradient to be defined by two parameters. The first is the principal field gradient, defined as $eq = V_{zz} = d^2V_z/dz^2$. In this case, the direction of the z-axis is defined by the orientation of the field created by the lattice with respect to the nucleus, not by an external laboratory frame. The second is the asymmetry parameter $\eta = \left(V_{xx} - V_{yy}\right)/V_{zz}$ which varies from 0 to 1, where 0 represents an axially symmetric

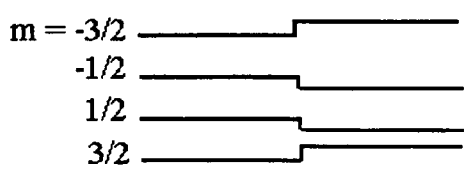

Figure 2.2. Perturbation of the Zeeman energy levels by the quadrupolar interaction.

field. The Hamiltonian for the quadrupolar interaction is then

$$H_Q = \frac{e^2qQ}{4I(2I-1)}\left\{3I^2{}_z - I(I+1) + \frac{1}{2}\eta\left(I_+{}^2 + I_-{}^2\right)\right\} \qquad \text{(Eqn. 2.8)}$$

where Q represents the quadrupole moment of the nucleus

In the presence of a large magnetic field, this Hamiltonian leads to NMR frequency shifts of first and second order in $\nu_Q = 3e^2qQ/2I(2I-1)h$. The first order shift is

$$\nu_{m\to m-1}{}^{(1)} = \nu_Q \frac{1}{2}\left(m - \frac{1}{2}\right)\left(3\cos^2\theta - 1 - \eta\cos 2\varphi \sin^2\theta\right). \qquad \text{(Eqn. 2.9)}$$

This creates what are commonly called quadrupolar satellites. The second order shift moves the primary resonance line and is given by

$$\nu_{m\to m-1}{}^{(2)} = \frac{\nu_Q{}^2}{12\nu_0}\left\{\begin{array}{l}\frac{3}{2}\sin^2\theta\left[(A+B)\cos^2\theta - B\right] + \eta\cos 2\varphi \sin^2\theta\left[(A+B)\cos^2\theta + B\right] \\ +\frac{\eta^2}{6}\left[A - (A+4B)\cos^2\theta - (A+B)\cos^2 2\varphi\left(\cos^2\theta - 1\right)^2\right]\end{array}\right\}$$

(Eqn. 2.10)

where

$$\begin{aligned} A &= 24m(m-1) - 4I(I+1) + 9 \\ B &= \frac{1}{4}\left[6m(m-1) - 2I(I+1) + 3\right] \end{aligned} \qquad \text{(Eqn. 2.11)}$$

θ is the angle between $\vec{H}_0$ and the principal axis of the electric field gradient, V_{zz}. φ is the angle between the x-y axis of the lab frame and the x-y axis of the principal axis frame.[8]

Of course, the resonance frequencies used in NQR, where there is no external magnetic field present, are not the same as those used in NMR, although both are typically

in the Megahertz range. The NQR transitions are between the spin ±3/2 and ±1/2 energy levels. The NQR frequency for I=3/2 is

$$\nu_{NQR} = \nu_Q\left(1+\frac{\eta^2}{3}\right)^{1/2}. \qquad \text{(Eqn. 2.12)}$$

Note that unless $\eta = 0$, ν_{NQR} does not equal ν_Q. Because of the first order effect of the electric field gradient, the quadrupolar satellite frequencies found in NMR are proportional to the resonance frequencies found in NQR.[9]

Experimentally, the time a pulse is applied to obtain an angle of magnetization is different for NMR and NQR. The angle of magnetization is $\theta = H_1\gamma tA$. For NMR, in absence of a quadrupole perturbation, A = 1, leading to the equation $\theta = H_1 t\gamma$ which was given in Sec. 2.2. For NQR or strongly quadrupole perturbed NMR, $A = \sqrt{I(I+1) - m(m-1)}$. For a spin 3/2 transition, $A = \sqrt{3}$.[7]

3. LITERATURE REVIEW

3.1 Previous NMR and NQR Studies of $YBa_2Cu_3O_7$

There has been a great deal of NMR and NQR work done on $YBa_2Cu_3O_{6+x}$, both above and below the critical temperature. There have been a number of works examining the effects of either temperature or oxygen content on $YBa_2Cu_3O_{6+x}$. Unfortunately, there are few studies that combine these two factors, especially above room temperature. A comparison of the various experiments is possible, but this does have limitations because of the variations in samples, even though nominally the same composition, can lead to differing results. Experiments that have involved temperature have examined its effect on the NQR frequency, the relaxation rates, and the Knight shift. To the best of my knowledge, no experiments have been performed above 550 K.[10] The NQR frequency and the relaxation rates have also been studied with respect to the oxygen content.

There are two stable isotopes of Cu that may be seen with NMR and NQR, ^{63}Cu and ^{65}Cu. ^{63}Cu has an abundance of 69% and a gyromagnetic ratio $\gamma = 12.089 MHz / T$. ^{65}Cu has an abundance ratio of 31% and a gyromagnetic ratio $\gamma = 11.285 MHz / T$. Most studies have only looked at the ^{63}Cu isotope because the higher abundance leads to a greater signal intensity. There are two different Cu sites in $YBa_2Cu_3O_7$, the Cu(2) site, which is actually two equivalent sites, and one Cu(1) site. (See Fig. 1.1 and Fig. 1.2) The NMR parameters found for these two sites are different.

A useful trait of the powdered $YBa_2Cu_3O_7$ material is that it has an anisotropic total susceptibility. This property makes it possible to orient the powdered material with

the c-axis parallel to an external magnetic field. By fixing an oriented sample in epoxy, it is possible to do NMR studies with $\vec{H}_0$ parallel or perpendicular to the c-axis.

The NQR frequencies change slightly with temperature. For the fully oxygenated material, the Cu(1) frequency increases and the Cu(2) frequency decreases with an increase in temperature. (See Fig. 3.1) These frequency shifts are assumed to be caused by slight changes in the lattice parameters as the temperature is increased.[11]

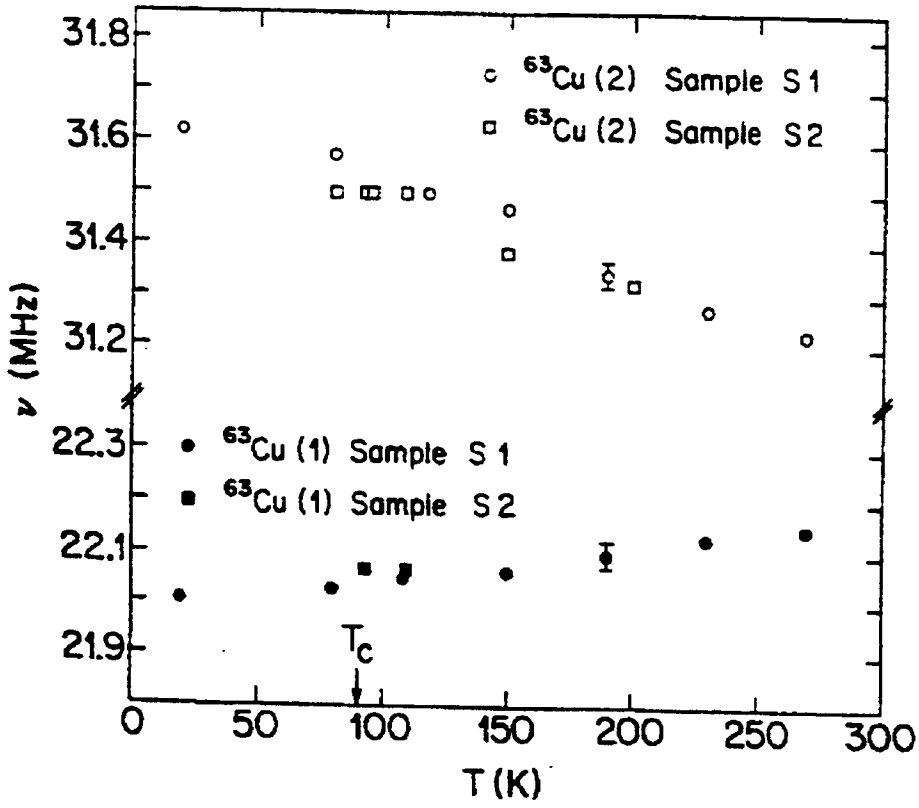

Figure 3.1. Temperature dependence of the ^{63}Cu NQR frequencies in $YBa_2Cu_3O_7$. The open points denote the Cu(2) sites; the closed points denote the Cu(1) sites. From ref. (12).

The dependence of the NQR frequency on oxygen content is far more complex however. As the oxygen content decreases, oxygen atoms are removed from the chain layer, creating Cu(1) sites that have a different number of Cu-O bonds. A Cu(1) site could have zero, one, or two chain oxygen neighbors with a different electric field gradient associated with each environment. This leads to different frequencies for the various Cu(1) sites. The oxygen deficiency also affects the Cu(2) sites, in part because of the change in bond lengths and the Cu positions. At room temperature in the fully oxygenated material, the Cu(1) site has two chain oxygens, or is four-fold co-ordinated, and has a NQR frequency around 22 MHz while the Cu(2) site has a frequency around 31 MHz. For the $O_{6.5}$ material, the two-fold co-ordinated Cu(1) site has a frequency around 31 MHz.[11,12,13] For the O_6 material, the two-fold co-ordinated Cu(1) site has a frequency around 30 MHz. It is very difficult to see the signal from the Cu(2) sites, around 23.5 MHz, due to the anti-ferromagnetic ordering.[14] It is difficult to label the frequencies conclusively for oxygen contents between these two extremes. As can be seen in Fig. 3.2, as the oxygen content decreases, the Cu(2) signal broadens and shifts downward in frequency, blurring the frequency distinction between the two copper isotopes. The lack of distinct lines is presumably caused by both the first neighbor effect of the Cu(1) atom in the unit cell and differences in neighboring unit cells. It has been estimated that one oxygen atom missing in the chain layer affects 12 Cu(1) sites and 24 Cu(2) sites.[12] Because the line shape broadens if defects and oxygen deficiencies are present, the quality of samples that are nominally O_7 are sometimes characterized by how narrow the NQR lines are.

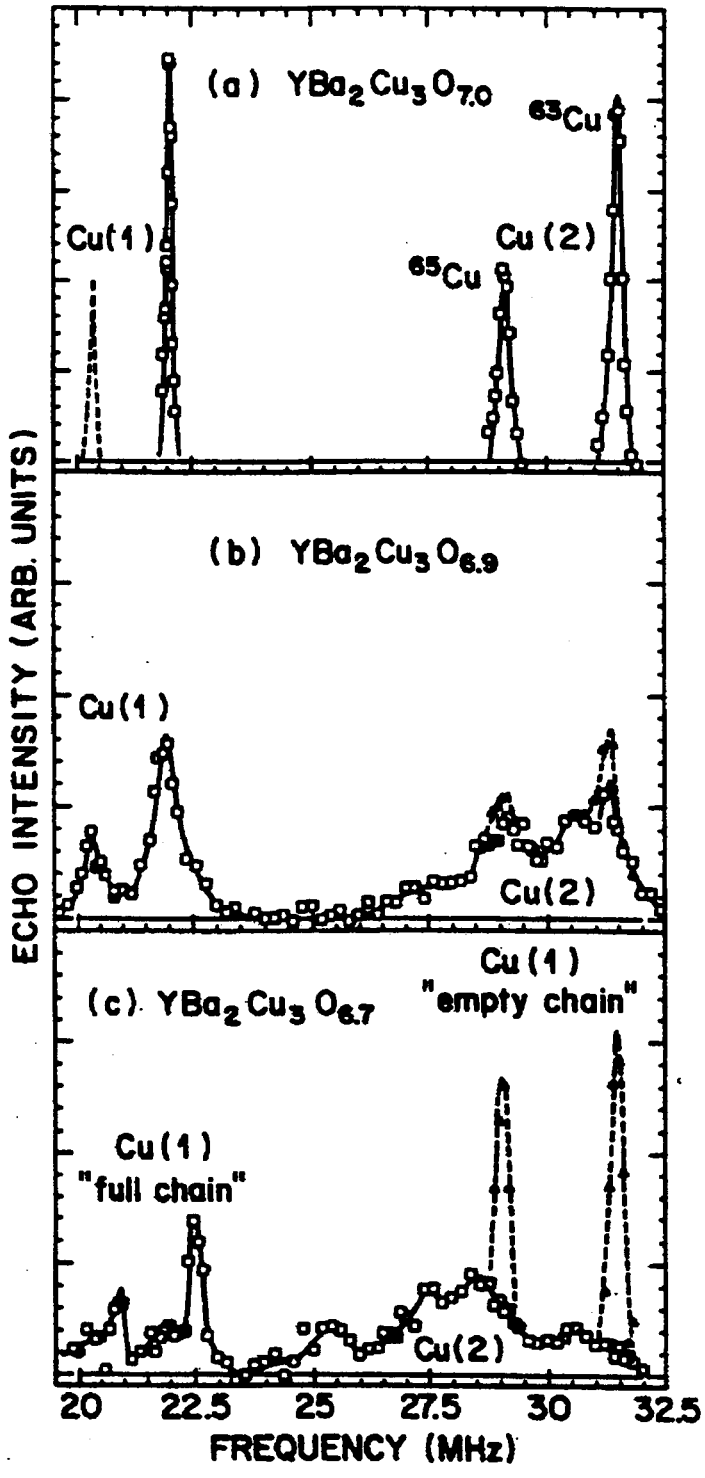

Figure 3.2. ^{63,65}Cu NQR spectra at 100 K for various oxygen concentrations. Open points denote the data taken using short pulse repetition rates (~100 Hz); closed points denote data taken using long pulse repetition rates (~ 1 Hz). From ref. (14).

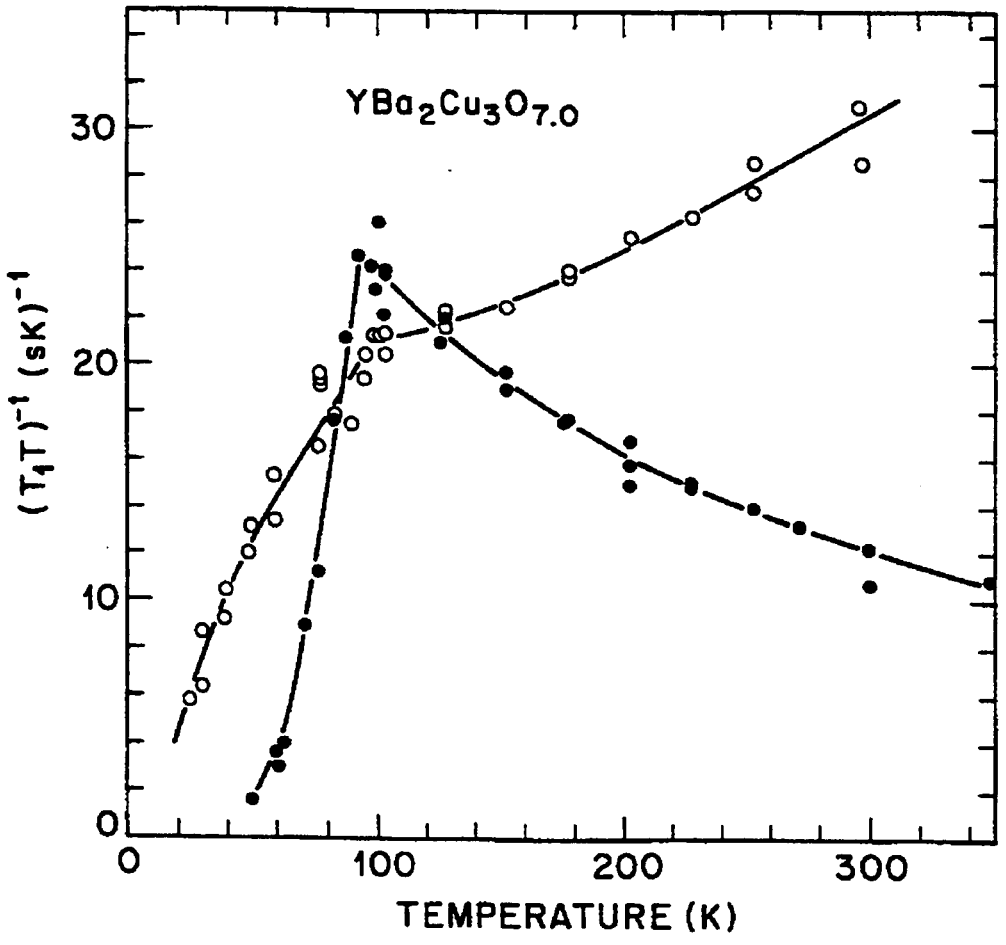

Figure 3.3. Temperature dependence of the ^{63}Cu NQR spin-lattice relaxation rate for $YBa_2Cu_3O_7$. Open points denote Cu(1); closed points denote Cu(2). From ref. (14).

The NQR spin-lattice relaxation rate's dependence on temperature is shown in Fig. 3.3. An example of the difference between a fully oxygenated sample and an oxygen deficient sample is shown in Fig. 3.4. The two-fold co-ordinated Cu(1) line has a T_1 that is of order one hundred times that of the 22 MHz line. (See Fig. 3.2)[13]

The NQR spin-spin relaxation at the Cu(2) site does not have a simple exponential time dependence, but has a Gaussian component which gives it the form

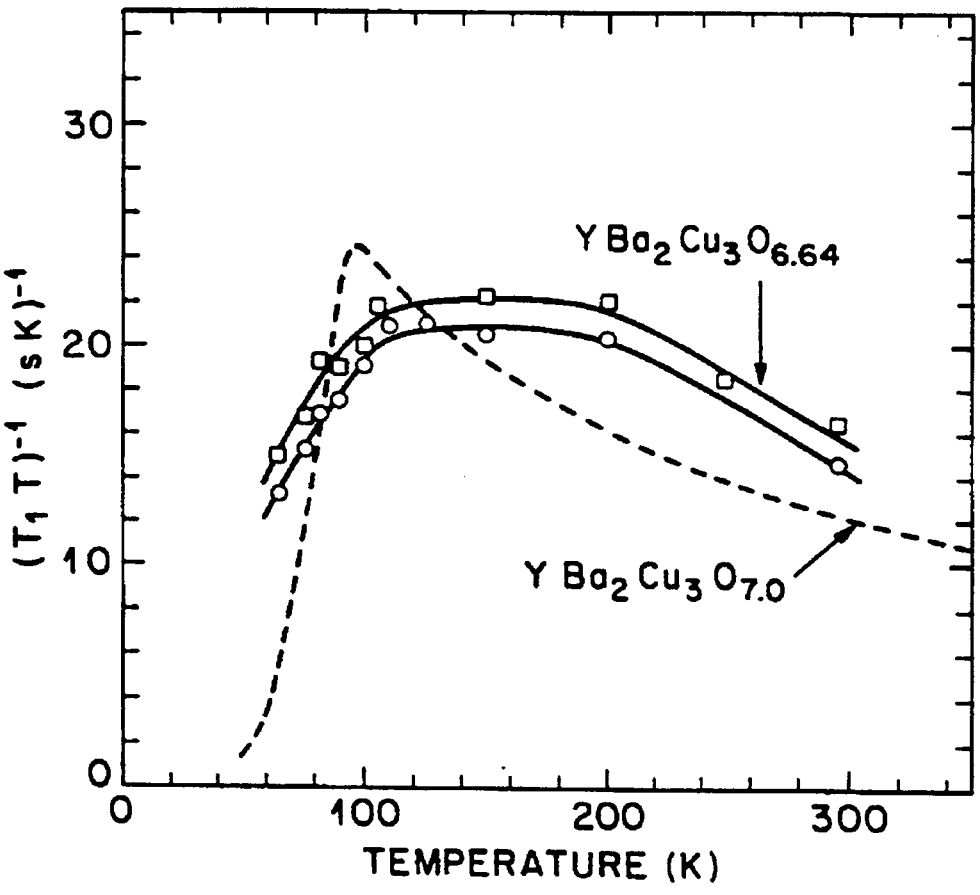

Figure 3.4. Temperature dependence of the ^{63}Cu(2) spin-lattice relaxation rate for two different oxygen stoichiometries. From ref. (14).

$$\exp\left(-\frac{t}{T_{2L}}-\frac{t^2}{T_{2G}{}^2}\right). \qquad \text{(Eqn. 3.1)}$$

The Gaussian component, T_{2G}^{-1}, decreases slightly with temperature and is somewhat dependent on $\vec{H}_1$. From Redfield theory, the Lorentzian component, T_{2L}, is related to the spin-lattice relaxation.[6] For the Cu(2) site, $T_{2L}^{-1} = T_1^{-1} * 3.7$.[15,16]

Table 3.1. Room temperature NMR and NQR parameters

	Cu(1)	Cu(2)	
ν_{nqr}	21.6 MHz	31.15 MHz	ref (12,14)
T_1	0.08 ms	0.280 ms	ref (11)
η	0.92	0.14	ref (12)
K (Knight Shift)	0.58	1.27 H parallel to c-axis	ref (18)
		0.58 H perpendicular to c-axis	

The Knight shift's dependence on temperature and oxygen has been studied. For the fully oxygenated material, the Knight shift is constant above the critical temperature. For oxygen deficient material, the Knight shift increases with temperature above T_c.[17]

For my experiments, it is useful to know the expected parameters for ^{63}Cu in the fully oxygenated material, $YBa_2Cu_3O_7$, at room temperature as determined by previous experiments. (See Table 3.1)

3.2 Oxygen Motion

Oxygen plays an important role in the superconductivity of $YBa_2Cu_3O_{6+x}$. There have been many studies that have used a variety of techniques to examine the motion of oxygen in an attempt to understand its behavior. Unfortunately, many times they raise more questions than they answer. Some of these questions arise from the fact that different techniques have different requirements and assumptions that go with them, such

as a difference in the definition of diffusion, creating conflicts when comparing results. Also, the declared stoichiometry will vary depending upon the method used to determine it. The material may also cause problems by creating shells or layers of different stochiometries, twinning, or changing over time.

3.2.1 Apical Oxygen Double Well[18,19,20]

The lattice vibrations have been studied using infra-red (IR) and Raman scattering. Each technique has some limitations caused by symmetry considerations, but together, they take a reasonably complete look at the vibrations of the oxygen bonds. The most controversial results have come from the IR studies. They have revealed the possibility of a "double well" for the apical oxygen. Some researchers have suggested that the apical oxygen has a double well potential, permitting the apical oxygen to have two possible

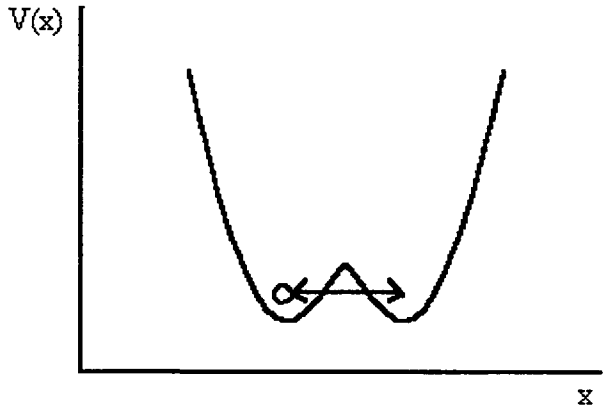

Figure 3.5. Apical oxygen double well potential.

positions that it tunnels between. (See Fig. 3.5) This effect is also seen by EXAFS (X-ray absorption fine structure), but it has not been seen by neutron diffraction or Raman studies. The positions are separated by about 0.13Å. Although Raman scattering has not observed this effect, it could be that the apical oxygens on either side of the Cu(1) site move together, with one bond shortening and the other lengthening. (See Fig. 3.6) If both bonds expanded and contracted together, Raman scattering would be able to observe the effect. EXAFS is sensitive to the instantaneous relative position of an atom with respect to a reference atom, in this case the Cu(1) atom, and so is able to distinguish between the two sites. Neutron scattering sees the average position of the atoms with respect to the entire crystal, and so would not distinguish between two positions that are equally populated. However, it should be able to observe from thermal broadening the

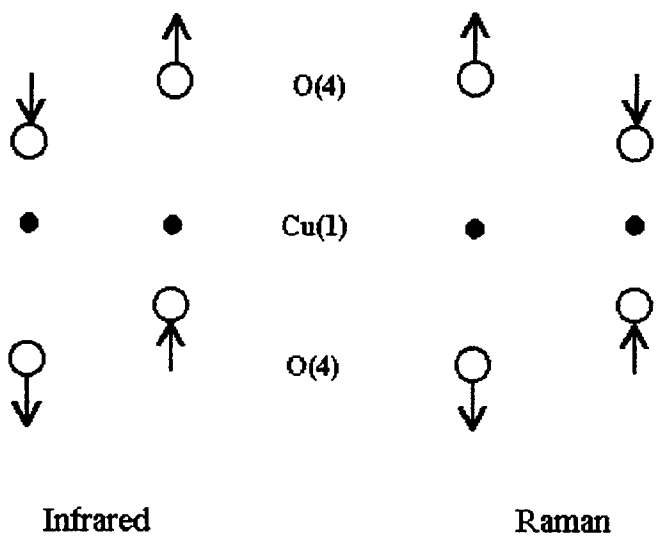

Figure 3.6. Cu-O vibrational modes capable of being seen by infrared and Raman studies.

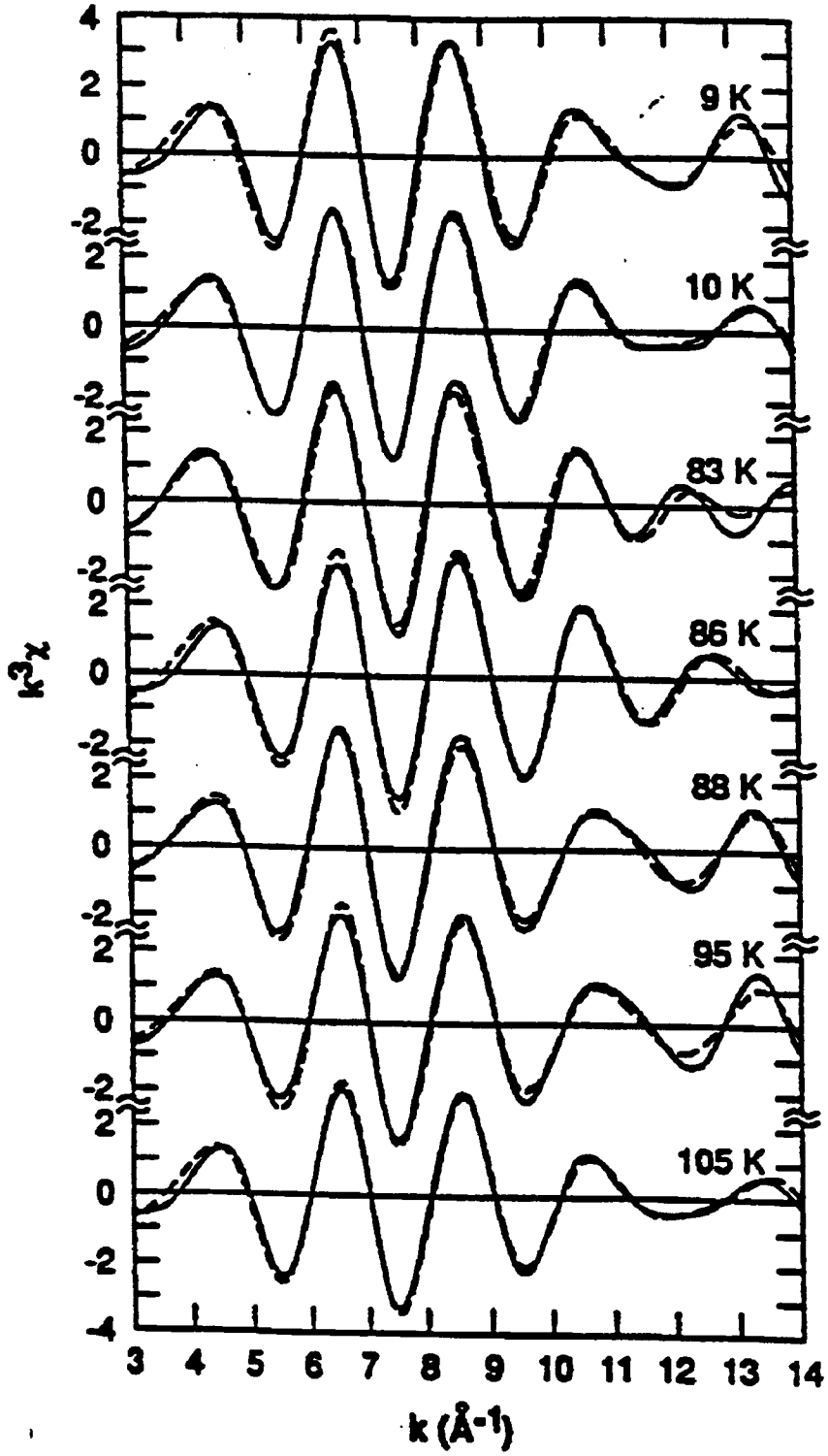

Figure 3.7. EXAFS spectra at various temperatures. Solid line denotes experimental data; dashed line is theoretical fit for a double well potential. From ref. (19).

range of positions where the oxygen atom might be. It has not seen any indication of the double well. This has created a considerable amount of debate about its existence. The double well has been observed from temperatures below T_c up to room temperature and in both the orthorhombic and tetragonal structures. Unfortunately, no one has yet done a study to determine if it disappears or changes above room temperature.

In addition to the existence of this double well, the behavior is observed to change near T_c. The EXAFS patterns show a beat as the temperature goes through T_c. (See Fig.3.7) However, the behavior both above and below T_c is the same. IR studies also show a similar behavior. It appears that the two apical oxygens move closer together near T_c. The double potential well would narrow as the temperature passes through T_c. The most puzzling feature of this double well is that it changes just at T_c, but appears to be the same both above and below T_c. It has also appeared in all other EXAFS studies of superconductors containing apical oxygens. There is some question about whether this effect is required for superconductivity or is simply a side effect.

3.2.2 Oxygen Ordering[1,2,3]

Near room temperature, several techniques, particularly neutron and electron diffraction, have observed ordering of the oxygen vacancies in oxygen deficient material. The primary structure seen in this ordering has been orthorhombic II, which was discussed earlier (See Sec. 1.1.1). It is believed that oxygen chain fragments form even at the lower oxygen stoichiometries. The ordering appears to increase the T_c for the lower oxygen

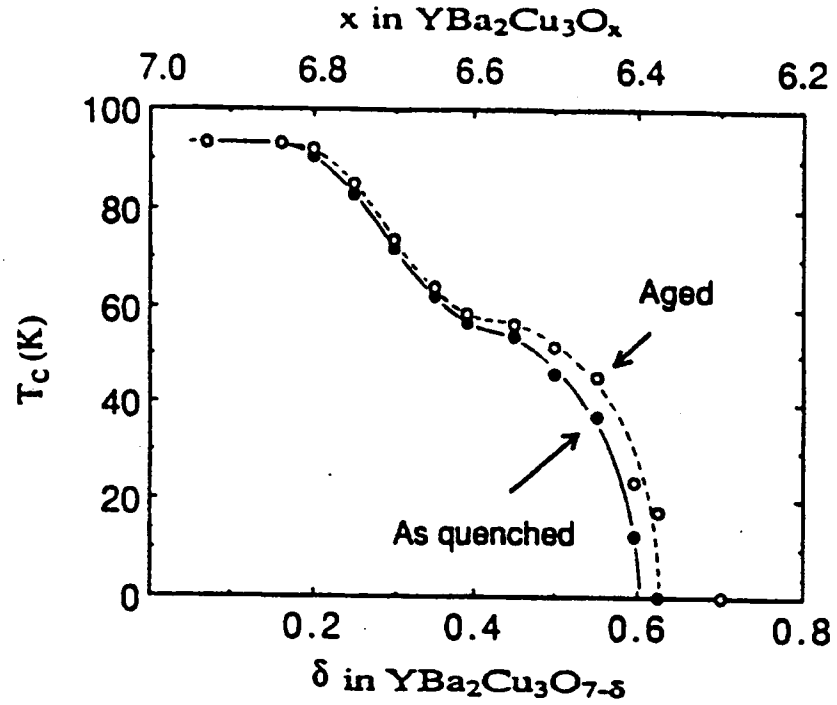

Figure 3.8. Dependence of T_c on oxygen stoichiometry immediately after quenching and after aging. From ref. (3).

concentrations and it is believed to be responsible for the 60K plateau that is seen in the oxygen content vs T_c graph. (See Fig. 1.5 and 3.8) The ordering of the oxygen into chains maximizes the number of fully co-ordinated Cu(1) sites, thus maximizing the carrier concentration in the planes. This ordering also makes the material more orthorhombic, increasing the difference between the lattice parameters a and b. There have been model calculations that show ordering of the oxygen and the oxygen vacancies to be energetically favorable.

This ordering is not seen at higher temperatures, but appears as the material anneals at lower temperatures. The lower the oxygen concentration, the more significant

is the change of T_c with aging, up to a change of 20K. (See Fig. 3.8) As the oxygen content is lowered below $O_{6.35}$, the material becomes tetragonal. It is thought that the chain fragments still exist, but are shorter and are randomly oriented. The randomness causes the average crystal structure to appear tetragonal, although locally it could be orthorhombic. Of course, as oxygen decreases down to O_6, the chains will completely disappear. Studies have also been done to examine the ordering at lower temperatures, which has yielded activation energies for the ordering. (See Table 3..2)

3.2.3 Internal Friction[21]

Internal friction, also known as mechanical loss measurement, is a technique that bridges the gap between small vibrations and bulk diffusion. It observes the energy dissipation of ultrasonic waves. Loss maxima are associated with a vibration or jump of an atom in the material. It is able to observe correlated atomic motion in which an atom returns to its original site after a hop. Internal friction can distinguish between thermally activated motion and motion induced by a phase transition. For thermally activated motion, if the material exhibits Arrhenius behavior, internal friction is able to provide information about the activation energy and the relaxation times associated with the motion. A behavior is said to be Arrhenius if it can be represented by the equation $\tau = \tau_0 \exp(E / kT)$, where τ is the relaxation time, τ_0 is the inverse of the attempt frequency, and E is the activation energy. (See Table 3.2) Fig. 3.9 shows the resonances seen for the frequencies 1 kHz and 1 Hz. A shift of the temperature at which a peak occurs with a change in frequency indicates a thermally activated motion.

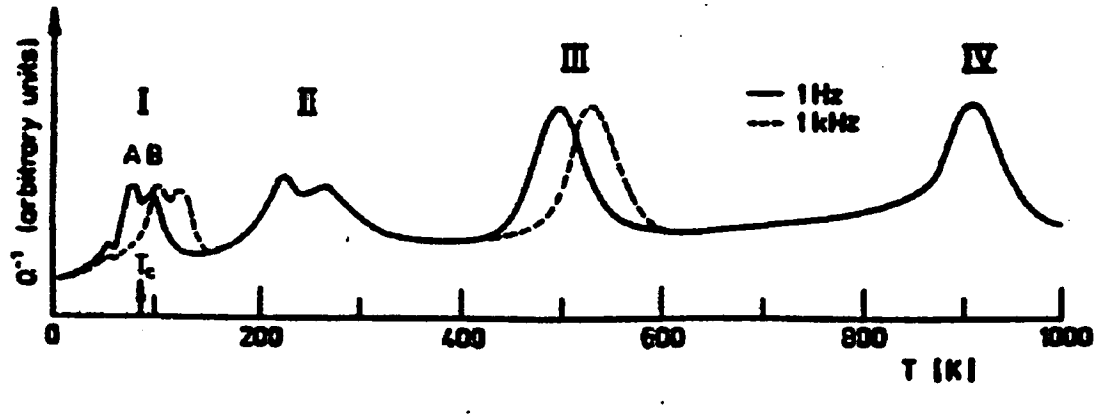

Figure 3.9. Internal friction loss maxima. From ref. (22).

Examining temperatures near T_c, there are three peaks, all thermally activated, and none associated with a phase transition at T_c. (See Fig. 3.10) Although the activation energies and relaxation rates have been found, there is little consensus on the interpretation of any of the peaks. However, there have been studies done on their dependence on the oxygen content. Peak C is associated with the tetragonal structure, and increases with decreasing oxygen.. Peak B is associated with the orthorhombic structure. Peak A is associated with both the orthorhombic and tetragonal structures. Both peak A and peak B increase with increasing oxygen content. (See Fig. 3.11) There are several theories that have been proposed for all three peaks, mostly involving motions related to defects, but no consensus has been reached. Unfortunately, not much progress has been made in making a connection between the internal friction and the Raman and IR studies.

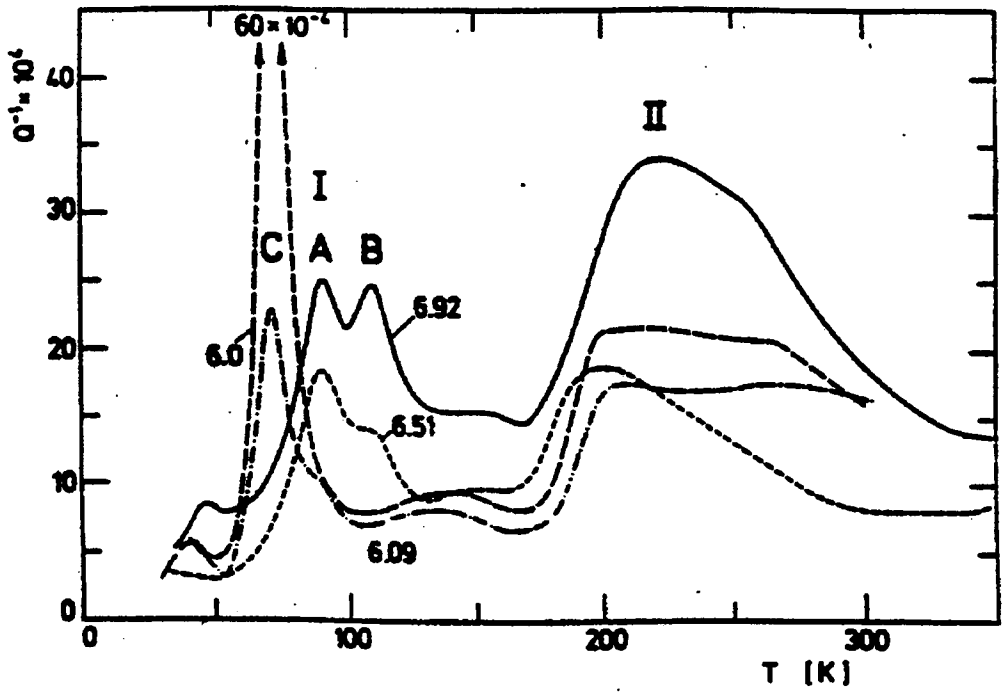

Figure 3.10. Internal friction loss maxima for different oxygen stoichiometries. From ref. (22).

Moving up in temperature, peak II has two components, one which is thermally activated and one which is appears to be a phase transition. The phase transition component occurs near 220K and is thought to be related to an order-disorder transition. However, there has been no other experimental evidence for this phase transition. There are many theories about the second component, several of which are conflicting. Unfortunately, it has not been examined in close enough detail to determine its activation energy or relaxation rate.

Peak III is believed to be caused by the thermally activated hopping of the oxygen atoms, or diffusion, in the chain layer via vacancies. It decreases when quenched from a

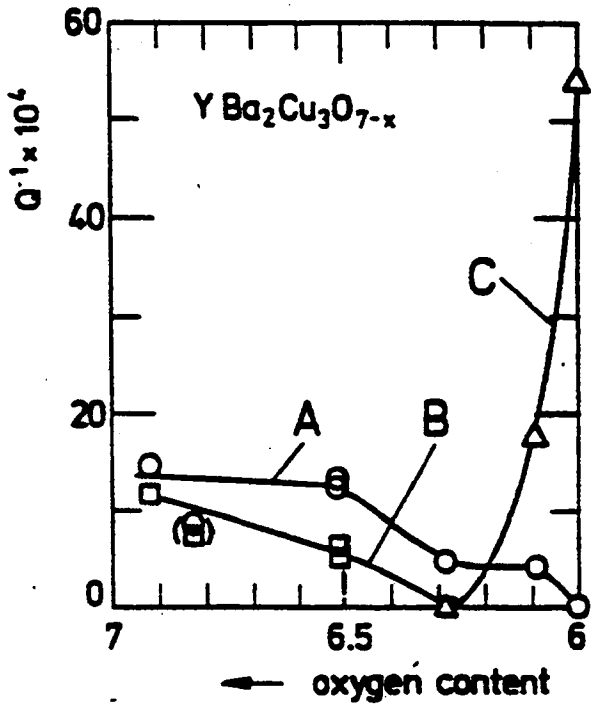

Figure 3.11. Dependence of magnitude of internal friction loss maxima on oxygen stoichiometry. From ref. (22).

high to low temperature and increases with aging which suggests that it may be related to ordering. This peak has also shown some indications that several processes could be taking place. This peak disappears as the oxygen content approaches O_6. Finally, near 900K, peak IV is associated with the motion that occurs during the phase transition between the orthorhombic and tetragonal structures.

3.2.4 Diffusion

At higher temperatures, oxygen is able to diffuse into and out of the material. By controlling the temperature and pressure, the oxygen content can be controlled.[22] (See

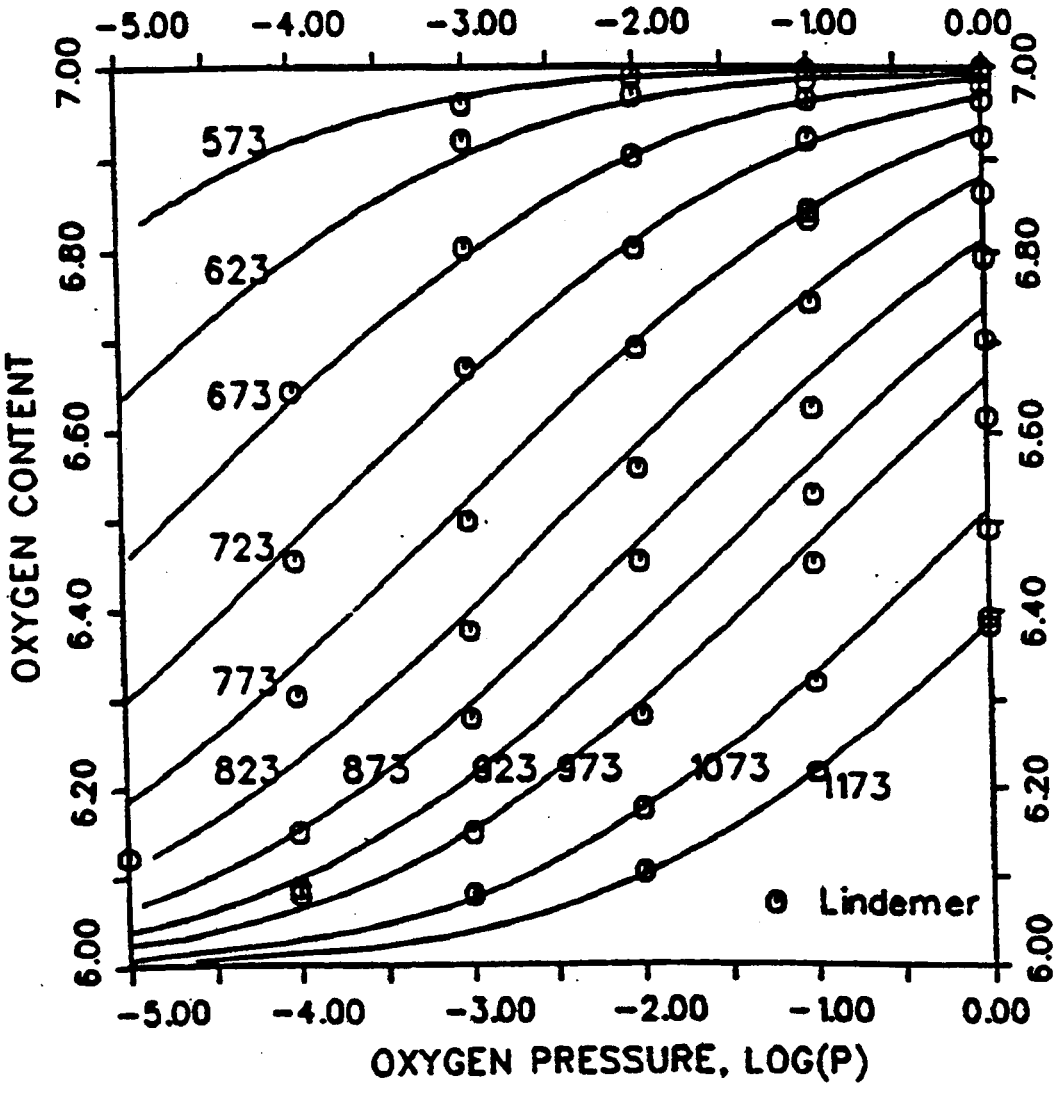

Figure 3.12. Dependence of oxygen content on pressure and oxygen pressure. From ref. (23).

Fig. 3.12) The diffusion of oxygen has been studied by many techniques, among them electrical resistance, tracer diffusion, and isotope gravimetrics. Unfortunately, the results from technique to technique are not consistent. This is partly due to the fact that there are two different types of diffusion. D^* is the tracer diffusion and is most closely related to diffusion of non-interacting point defects. $\tilde{D}$ is the chemical diffusion and includes the diffusion that occurs when there exists a chemical potential such as a pressure gradient. They are related by the equation, $\tilde{D} = D^*(1+\partial \ln\gamma / \partial \ln c)$ where $\partial \ln\gamma / \partial \ln c$ is thethermodynamic factor and γ is the activity coefficient. γ can depend on factors such as the oxygen stoichiometry and temperature. Another equation that is related to diffusion is $D = \Gamma x^2 f / 6$ where x is the jump distance, Γ is the jump frequency, and f is the correlation factor or the probability that the oxygen will not return to its original site. Theorists use these equations in trying to determine what happens during oxygen diffusion. Aside from the differences in the definition of diffusion, results may also vary because of material variations. Surface effects abound and the microstructure can be different from sample to sample, causing misleading results.[23,24,25,26,27,28]

Even given the variations in results, some information has been gained. Diffusion in the c-direction is far less, a factor of 10^6, than diffusion parallel to the a-b plane. Diffusion in the b-direction tends to be less, up to a factor of ten, than that in the a-direction. This suggests that diffusion occurs along the chains. Unexpectedly, the diffusion shows little, if any, dependence on the oxygen partial pressure. This is perhaps understandable if only the oxygen at the end of the oxygen chains is mobile. At the phase transition between the orthorhombic and tetragonal structures, near 900°K, no change was

seen in the diffusion behavior. Experiments examining the dependence of diffusion on the oxygen stoichiometry has yielded conflicting results, however.[28,29]

A study by Konder used oxygen isotopes to examine which oxygen atoms were diffusing at different temperatures. By examining the diffusion rates at different temperatures and the percentage of oxygen atoms exchanged, a closer look at what is happening is possible. Only the chain oxygens move below ~300°C. Between ~300°C and ~400°C, the chain and apical oxygens undergo diffusion. Above ~400°C, all of the oxygen atoms are involved in the diffusion of the isotope.[26]

Table 3.2. Activation energies and attempt times for oxygen motion

INTERNAL FRICTION	A	H = 0.13eV	$\tau_0 = 6.8 \times 10^{-12}$s
	B	H = 0.18eV	$\tau_0 = 1.0 \times 10^{-13}$s
M. Weller, ref. (22)	C	H = 0.08eV	$\tau_0 = 1.6 \times 10^{-10}$s
	III	H = 1eV	$\tau_0 = 10^{-13}$s
DIFFUSION			
B.W. Veal, ref. (3)		H = 0.96eV	$\tau_0 = 1.4 \times 10^{-12}$s
J.R. La Graff, ref. (30)		H = 0.4 - 1.10eV	in
		H = 0.5 - 0.6eV	out
K.N. Tu, ref. (26)		H = 0.71eV	in
K. Konder, ref. (27)		H = 0.71eV	chains
		H = 1.88eV	apical, planes

3.2.5 Possible Oxygen Jumps[30]

The information that has resulted from the assorted experiments has created a number of theories on oxygen motion, but not a great deal of consensus. There are two ways of treating the $YBa_2Cu_3O_{6+x}$ structure and the oxygen motion. One way is to treat the O_6 structure as the base structure and the O(1) and O(5) sites as interstitials. A more popular way is to use the O_7 structure and only think of the O(5) sites as interstitials.

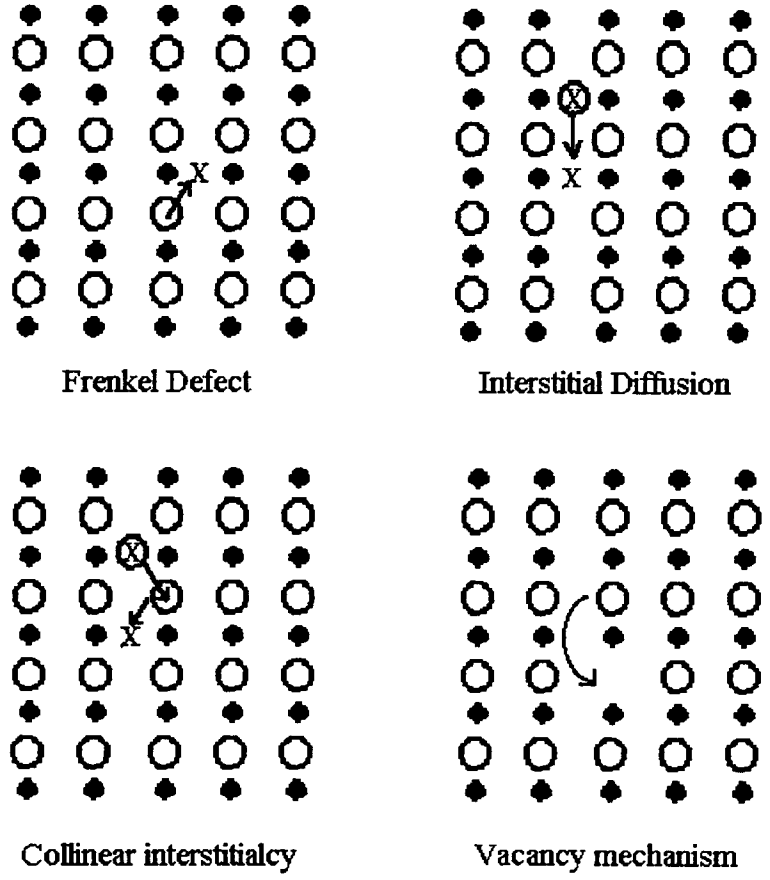

Figure 3.13. Possible oxygen jumps in the Cu-O chain layer.

There are four types of possible oxygen jumps in the Cu-O chain layer to consider: 1. O(1)-O(5) jump, sometimes called a Frenkel defect. 2. O(5)-O(5) jump, or interstitial diffusion. 3. O(5)-O(1) displacing the original O(1) atom to another O(5) site, called a collinear interstitialcy mechanism. 4. O(1)-O(1) jump, or diffusion by a vacancy mechanism. (See Fig. 3.13) Theoretical energy calculations have suggested that it is easier for an oxygen atom to hop to a non-chain end site, either O(1) or O(5), if there are vacancies present in the chain. The vacancies decrease the repulsion the oxygen feels from other oxygens.

4. DETAILS OF THE EXPERIMENT

4.1 Pulsed NMR Spectrometer

Although the NQR and NMR experiments were performed on two separate spectrometers, the fundamental system is the same for both. (See Fig. 4.1) The sample coil serves two purposes. It provides the applied radio-frequency magnetic field, H_1, parallel to its axis and acts as the pickup coil for the transverse magnetization signal from the sample. The radio frequency (RF) source is used to induce the magnetic field in the coil. In pulsed NMR or NQR, H_1 is applied for brief amounts of time. These pulses are controlled by a gate. The matching network is used to optimize the power transmitted for the frequency being used and to de-couple the transmitter from the receiver. After the

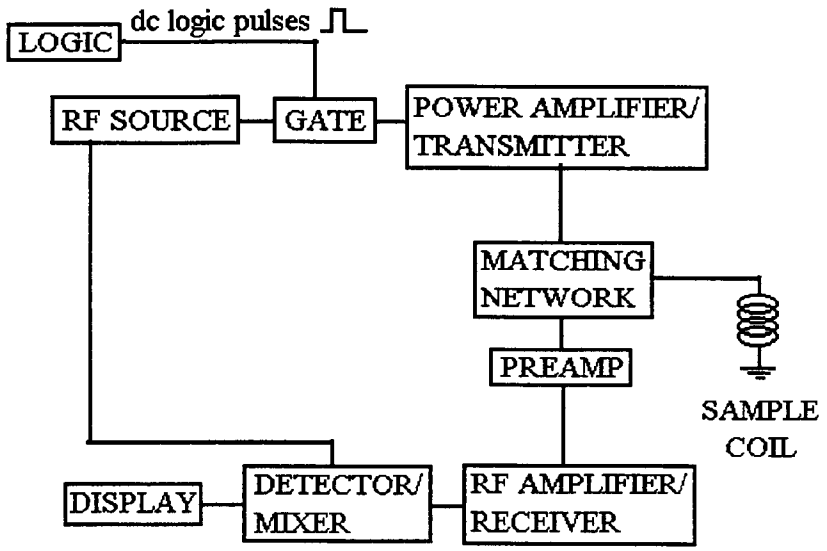

Figure 4.1. Pulse spectrometer block diagram.

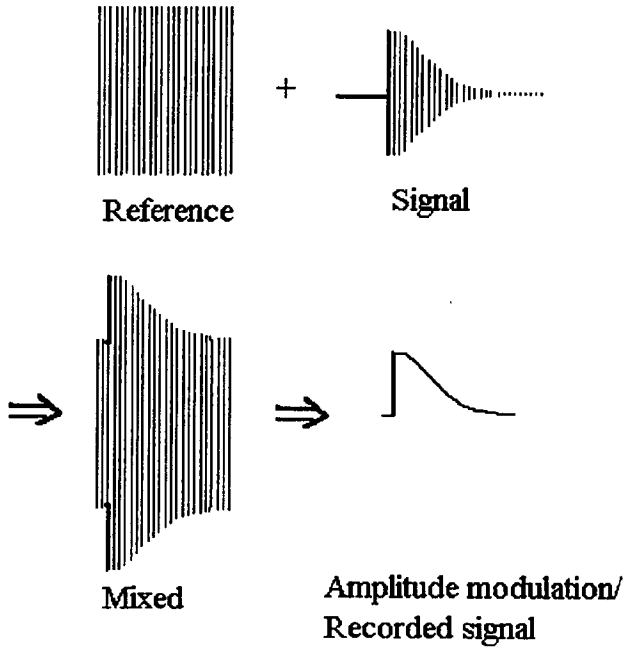

Figure 4.2. Signal detection using mixing.

signal from the sample is amplified, it is mixed with the RF source. The amplitude modulation is then detected and the resultant signal is digitized and stored. (See Fig. 4.2) Signal averaging is used to obtain an acceptable signal to noise ratio.

4.1.1 ATT Spectrometer

The ATT spectrometer was used for the NQR experiments. Although the spectrometer was used only for NQR, there is a 2 T iron-core magnet available for NMR experiments. It is a system designed and built by Dr. William W. Warren, Jr. while at ATT Bell Labs. The logic conditions for the pulses are controlled by altering the wiring and timings by hand. Because there are several coils and frequency ranges used, there are

several tune boxes, or matching networks. The matching networks were designed and built by Show-Jye Cheng and myself.

To optimize the system for a given frequency requires several steps. The matching network (See Fig. 4.3) has a variable capacitor in series with the coil which is tuned to provide a maximum signal output. A $\lambda/4$ cable connecting the transmitter to the coil is used to maximize the power transmitted. This cable acts as an impedance transformer between the transmitter's high impedance and the low impedance of the coil and matching network. To obtain the maximum signal, the RF source which will be mixed with the coil's output must have its phase adjusted by using a phase shifter. A phase difference of 0° or 180° will give a maximum signal, while a 90° phase difference will yield a minimum signal. This phase adjustment is often done by using a proton source in a magnetic field. The proton signal is large enough to see on an oscilloscope. This technique is particularly useful if the sample to be tested has a very small signal which requires signal averaging in order to be seen.

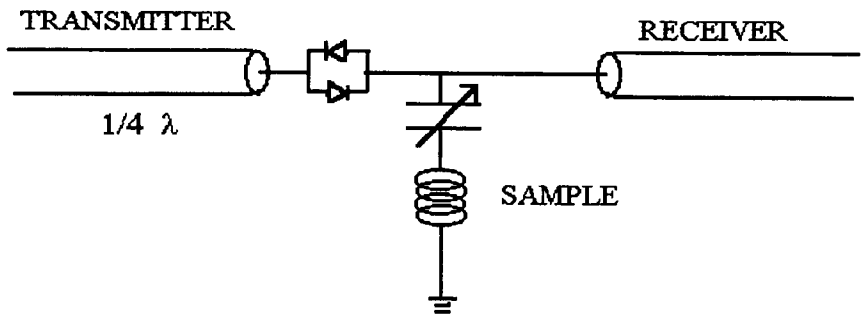

Figure 4.3. ATT spectrometer matching network.

To confirm that the system's behavior was consistent over the temperature range to be used, the system was checked using Cu_2O above room temperature. The $YBa_2Cu_3O_7$ Reference sample was used to check the system below room temperature. There was no obvious temperature dependence present.

4.1.2 Chemagnetics Spectrometer

A Chemagnetics CMX360-1436 spectrometer and an 8 T American Magnetics superconducting magnet were used for the NMR experiments. The CMX spectrometer is software driven, with all of the pulse logic conditions controlled by computer programs. The coils and matching networks are part of an integrated unit, or probe, to be inserted into the bore of the magnet. The probe used was designed and built by Show-Jye Cheng. The coil is oriented with its axis perpendicular to H_0, which has a value of 8 T.

Optimizing the CMX system involves tuning the matching network for the frequency desired. (See Fig. 4.4) The tune capacitor, a variable capacitor in parallel with the coil, tunes the parallel part of the circuit for the given frequency. The matching

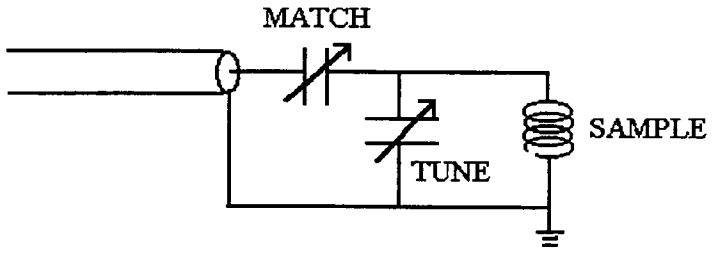

Figure 4.4. CMX spectrometer matching network.

capacitor is a variable capacitor used to match the impedance of the transmitter. Both capacitors must be adjusted simultaneously to minimize the reflected power from the probe.

The CMX system uses quadrature detection, which eliminates the need for manual phase adjustment. The output signal from the coil is mixed separately with two different RF signals which are 90° out of phase with each other. This creates two components of the signal which are orthogonal to each other. The sum of the squares of the two components then gives the magnitude of the signal.

4.2 Temperature Control

A hot air flow furnace is used for NQR studies above room temperature. (See Fig. 4.5) The heater elements warm a flow of air, which then flows over the sealed sample cell. The temperature is regulated by the use of a chromel-alumel thermocouple, an Eurotherm temperature controller and two dc power supplies in series. (See Fig 4.6) The outside of the furnace is kept cool by a flow of water. The furnace may be used up to 500°C.

For NQR studies below room temperature, a chilled air source is used. An FTS air dryer and cooler are used to bring the temperature down to -65°C. The air is then sent through a heat exchanger made up of metal coils placed in liquid nitrogen. The temperature control is the same as the one used above room temperature, with liquid nitrogen providing the reference temperature.

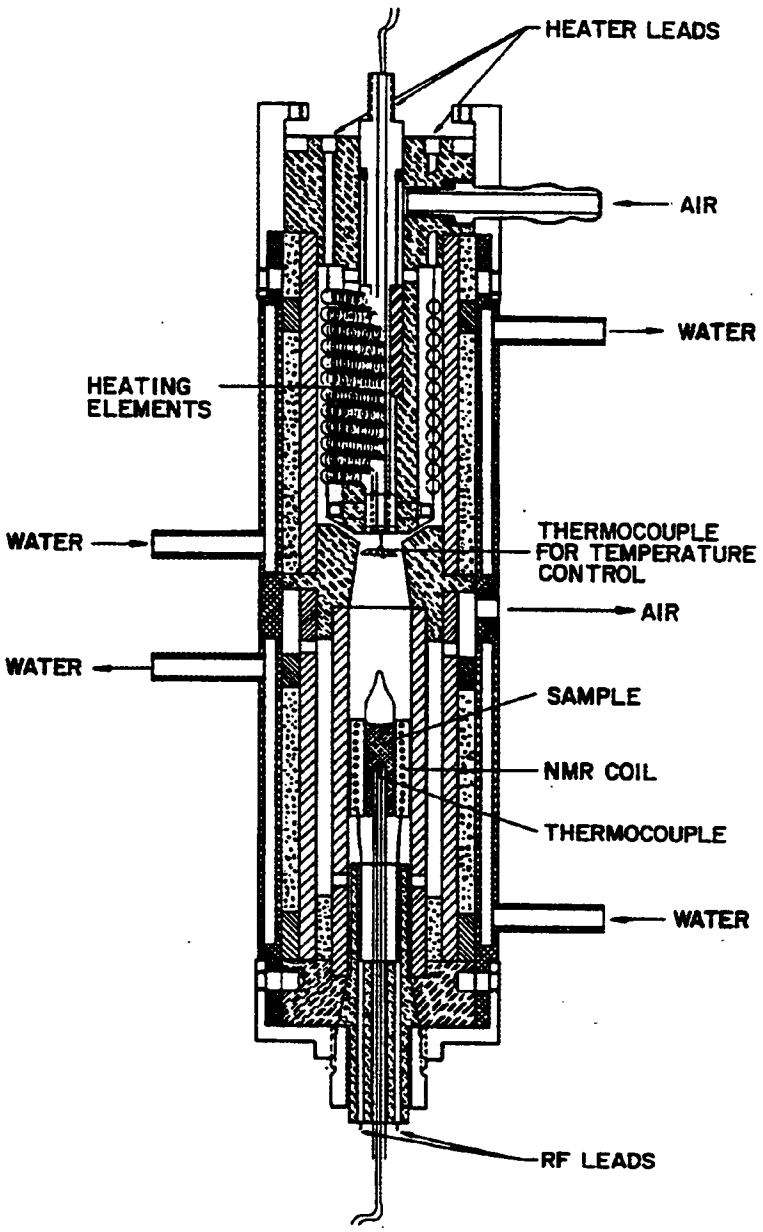

Figure 4.5. NQR hot air flow furnace.

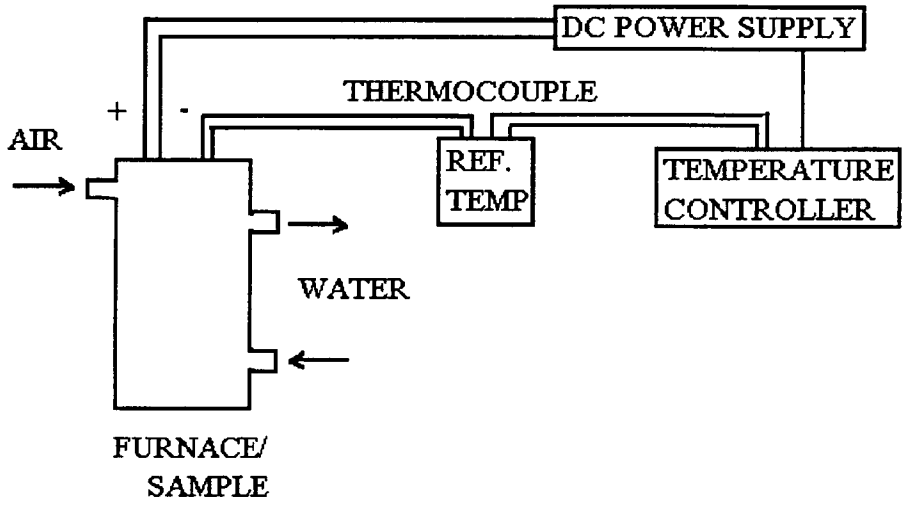

Figure 4.6. Furnace block diagram.

The CMX system also uses an air flow system, which is supplied by the manufacturer. The air supply is the same as that used for the NQR studies.

4.3 Data Analysis

4.3.1 Spin Echoes

In my experiments, spin echoes were used to obtain the data for both the NMR and NQR studies. I will only discuss how NMR spin echoes are obtained in a inhomogeneous magnetic field. The theory behind NQR spin echoes is similar and the experimental method used to obtain them is identical to that used in NMR.

4.3.1.1 Theory[6]

When a 90° pulse is applied, the net magnetization of the nuclei orients in the x-y plane. The net magnetization will be precessing at a rate ω_0 in the x-y plane. Switching to a rotating frame that is rotating a a rate ω_0, the net magnetization will be static along the positive x-axis. (See Fig. 4.7) Because of local differences in field, the nuclei will precess at slightly different rates in the x-y plane, causing them to lose their phase coherence. This creates a decaying signal called a free induction decay (FID). If at time τ, a 180° pulse is applied, the net magnetization will be inverted. The net magnetization is now along the negative x-axis and the direction of rotation has reversed. Each nucleus has the same rate of precession that it had after the 90° pulse. Effectively, the spins have changed direction and are returning to their starting point. At a time τ after the 180° pulse, the spins will regain the phase coherence that they had immediately following the 90° pulse. As happened immediately after the 90° pulse, the spins will again begin to dephase. The signal seen as phase coherence is reached is called a spin echo. It is essentially two free induction decays placed back to back.

The observed spin echo signal will become smaller as τ is increased due to T_2 processes. In order for the spin echo to occur, the spins must have the same precession rate before and after the 180° pulse. If for any reason the local environment around a nucleus changes, causing its precession rate to change, it will no longer contribute to the spin echo.

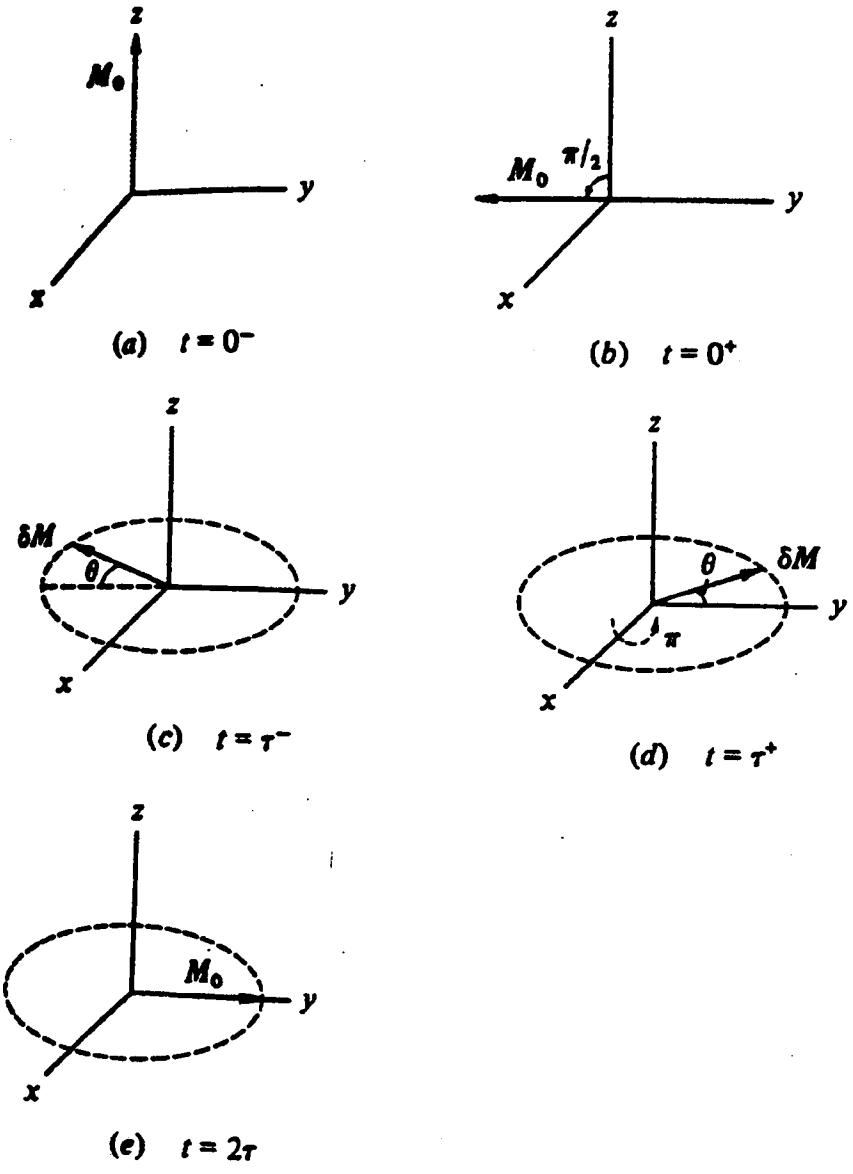

Figure 4.7. Formation of a spin echo by using a $\pi/2$ - π pulse sequence. (a) Magnetization at thermal equilibrium along z-axis. (b) Magnetization in -y direction immediately following $\pi/2$ pulse. (c) Part of magnetization has precessed an extra angle due to imhomogeneities. (d) Effect of π pulse at $t = \tau$ on δM. (e) At time 2τ, magnetization has refocused in +y direction. From ref. (7).

The advantage of observing spin echoes instead of the FID is that it is possible to avoid some of the side-effects that the pulse has on the electronics of the system. An example is the dead time during and after the pulse which is necessary for the preamp to recover from the pulse. By observing the spin echo, the dead time does not interfere with the data. However, because of T_2 processes, the spin echo signal will be smaller than the original FID.

4.3.1.2 ATT Spectrometer

To optimize the signal seen, the 90° and 180° pulses need to be adjusted. The angle that the pulse will rotate through is $\gamma H_1 t$ for NMR and $H_1 \gamma t\sqrt{3}$ for NQR, where t is the duration of the pulse. (See Sec. 2.2 and Sec. 2.5.2) The H_1 is determined by the power transmitted to the coil. Because that power will differ for different coils, the time required for a 90° or 180° pulse must be found for each individual coil. If the gate sends out a perfect pulse that has a square shape, the time for the 180° pulse will be twice that of the 90° pulse. In this system, however, the gated pulse has a rise time. This causes the time for the 180° pulse to be slightly less than that for the 90° pulse, requiring that both pulses be optimized separately. Because the NQR pulse widths required for the Cu atoms in $Y_1Ba_2Cu_3O_7$ are about twice that of the NMR pulse width for protons in the same coil, it is sometimes convenient to get an estimate of the pulse widths while using protons in a magnetic field to optimize the phase for the coil. This is particularly useful when working with a new coil.

Because of the coherent noise problems that are created by the electronic ringing of the coil, it was necessary to do a four part pulse sequence to acquire the data. (See Fig. 4.8) Two different τ values were used, which led to two spin echoes. The τ values used were 25 μs and 40 μs. The entire four part sequence was repeated as often as was necessary to obtain the signal to noise ratio desired. To allow the longitudinal magnetization to relax, the typical repetition rate is usually $3 \times T_1$. However, because of the transmitter's power output limitations, the repetition rate used was 100 Hz. The data was then digitized and both spin echos integrated.

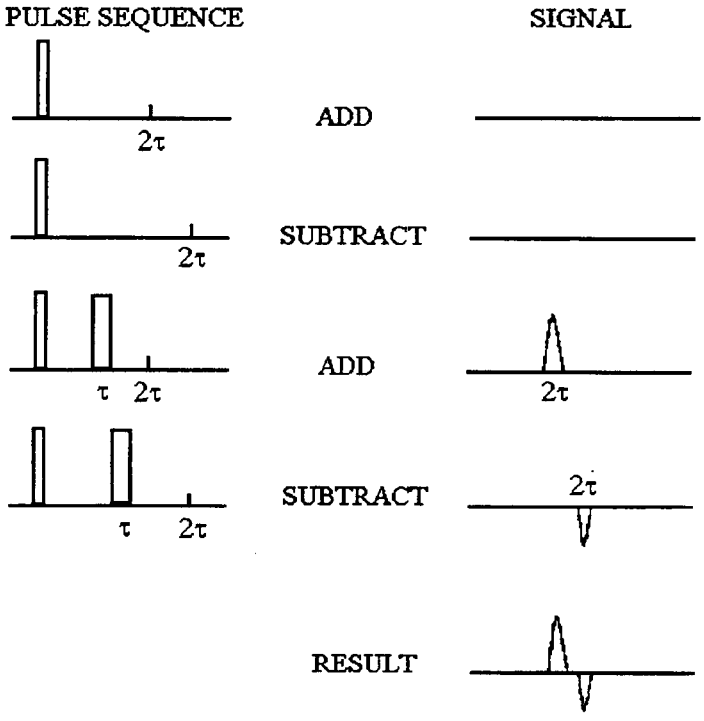

Figure 4.8. NQR pulse sequence.

4.3.1.3 CMX Spectrometer

Because the reference signal is phase cycled, this spectrometer experiences less electronic ringing, making a single spin echo pulse sequence practical. The gated pulses for this system are quite close to being square pulses, so the time used for the 180° pulse is twice that of the 90° pulse. The τ value used was 20 μs. The pulse width conditions for the coils that were used were determined by Show-Jye Cheng. The spin echo pulse sequence was repeated at a repetition rate of 100 Hz until the signal to noise ratio was satisfactory. The two components of the signal were then squared and added, then the square root was taken. The result is the modulus of the signal and may be calculated because the two signals are 90° out of phase. The amplitude of this signal was then found.

4.3.2 Spectra

If the line width of the spectrum is larger than the inverse pulse width, the true line shape of the spectrum will not be seen by a Fourier transform of the FID or the spin echo signal. It is then necessary to provide a rough Fourier transform by plotting the spectrum point by point by plotting either the intensity or the amplitude of the signal against the frequency. As $YBa_2Cu_3O_{6+x}$ has a broad spectrum, this technique was used. For the temperature analysis, the integrated values of the spectra were used to obtain the signal intensity. The intensity multiplied by the temperature, in Kelvin, was then plotted against the temperature.

4.3.2.1 NQR Spectra

The NQR spectra were created by plotting the integrated values of the spin echoes against the frequency. The resonance frequencies expected are known from the literature. (See Sec. 3.1) To adequately display the line shape, the frequency step used was 0.03MHz.

4.3.2.2 NMR Spectra

The NMR spectra were created by plotting the amplitude of the spin echoes. Because the resonance frequency depends on the magnetic field, the expected frequencies needed to be calculated. As the powdered $YBa_2Cu_3O_7$ samples partially orient with the c-axis parallel to the magnetic field, the spectra are expected to be a superposition of a broad powder pattern and the narrower peaks associated with the oriented material. A permanently oriented sample could be aligned with the c-axis either parallel or perpendicular to the magnetic field..

Using the parameters found in the literature (Sec. 3.1) and eqns. 2.9-11 for the quadrupole shifts it is possible to calculate the expected positions of the major peaks in the spectrum. My calculations are intended only to determine the general location and identification of the various peaks. Although there are two spectra for the two different Cu isotopes, the main spectra do not overlap. I used the ^{63}Cu isotope in my experiment. I approximated $\eta = 1$ for the Cu(1) site and $\eta = 0$ for the Cu(2) site. The powder pattern

has two peaks associated with the Cu(2) nuclei at 86.63 and 92.32 MHz. The Cu(1) site has one peak located at 90.27 MHz. Fig. 4.9 shows a theoretical powder pattern with its dependence on η.

For the oriented material aligned with the c-axis parallel to the magnetic field, there are two peaks associated with the Cu(1) site. The spin 1/2 transition has a frequency of 92.13 MHz. The quadrupolar satellite, or spin 3/2 transition is expected at 90.79 MHz. The Cu(2) site has one spin 1/2 transition and two quadrupolar satellites. The spin 1/2 transition is at 91.42 MHz and the two satellites are expected at 60.02 and 122.82 MHz.

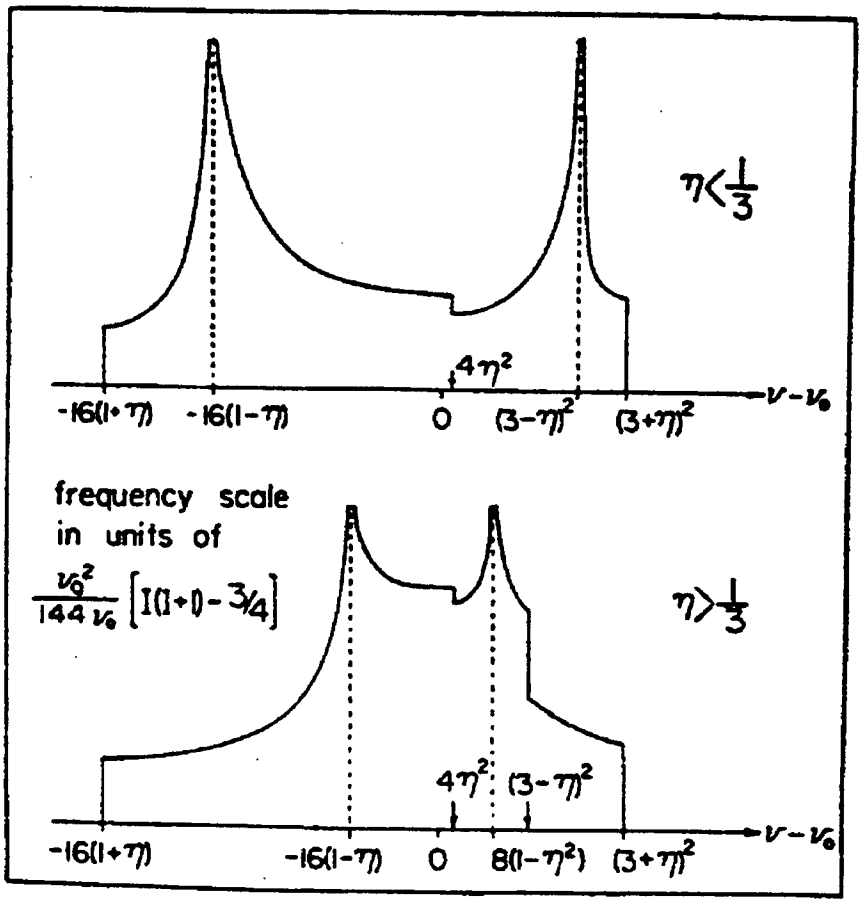

Figure 4.9. Theoretical NMR powder pattern for I = 3/2. From ref. (32).[31]

For the oriented material aligned with the c-axis perpendicular to the magnetic field, there is a spin 1/2 transition, at 92.83 MHz, and two quadrupolar satellites, at 82.30 and 112.25 MHz, associated with the Cu(2) site. The Cu(1) site does not have distinct lines because there is no orientational distinction between the a and b axis.

The step frequency was varied, using smaller frequency steps at the peaks to define the structure and larger frequency steps where there was little or no structure.

4.3.3 T_2 Studies

To study T_2, the τ value between the 90° and 180° pulses was varied. The log of the integrated spin echo value is then plotted against the time 2τ. The primary difficulty in obtaining this data is that as τ gets longer, the spin echo gets smaller. This requires an increase in the number of data acquisitions to maintain a reasonable signal to noise ratio.

4.4 Sample Preparation

The $YBa_2Cu_3O_7$ samples, with the exception of the reference sample, were made by Dr. Arthur Sleight's research group at Oregon State University's Chemistry Department. The reference sample was made by R.J. Cava at AT&T Bell Laboratories. The Sleight samples were prepared using Y_2O_3, $BaCO_3$, and CuO. The powders were ground together, pelleted, and heated at 850°C in air for 16 hours. The powder was then reground and heated at 950°C in air for 16 hours. This step was repeated. Then the powder was reground, pelleted and heated at 1000°C in air for 16 hours. The powder was

ground and pelleted again and heated in O_2 for 48 hours, then cooled to 25°C at 1°/min under O_2.

The samples were characterized by X-ray diffraction, which indicated that there was no second phase (less than 1%). The samples were also characterized by ac susceptibility tests. The samples used in my study had critical temperatures of 92 K.

The samples were then checked by using NQR. (See Sec. 5.1) Because $YBa_2Cu_3O_7$ reacts to the presence of water in the air, the samples were kept with Drierite or were sealed in sample cells. Because the temperature range that would be used was unknown, the initial samples were sealed in quartz tubes. Later samples were sealed in Pyrex. Except for the sample Poor-Vacuum which was sealed in a 10^{-5} Torr vacuum, all samples were sealed with 0.5-1.0 atmospheres of O_2. This oxygen pressure ensured that oxygen would not diffuse out of the material. (See Sec. 3.2.4)

Table 4.1. Labels for samples used

SAMPLE	LAB LABLE AND COMMENTS
Reference	Cava-5
Good	AWS-4b oxygen
Fair	AWS-122794aoxygen
Poor-Vacuum	AWS-111993avacuum
Poor-Oxygen	AWS-042694 oxygen
Oriented	silicon epoxy

The sample Oriented, after an initial NMR powder spectrum, was used to make an oriented sample. The powder was ground as fine as possible. It was then mixed with an Emerson and Cuming epoxy in a 3:7 ratio (Eccosil 4640 white silicone and Catalyst 50) and allowed to harden overnight in the 8 T magnet. This created a sample with the majority of the crystals aligned with the c-axis parallel to the magnetic field. Because most epoxies are not rated for higher temperatures, I used a silicon based epoxy rated for the temperature range I needed. However, this epoxy had not been previously used with $YBa_2Cu_3O_{6+x}$ and the possible effects on the material were unknown.

5. RESULTS

5.1 Initial Characterization of Samples

The $YBa_2Cu_3O_7$ samples were initially characterized using NQR at room temperature. The Cu(2) site was examined in all samples. (See Fig. 5.1) The Cu(1) site

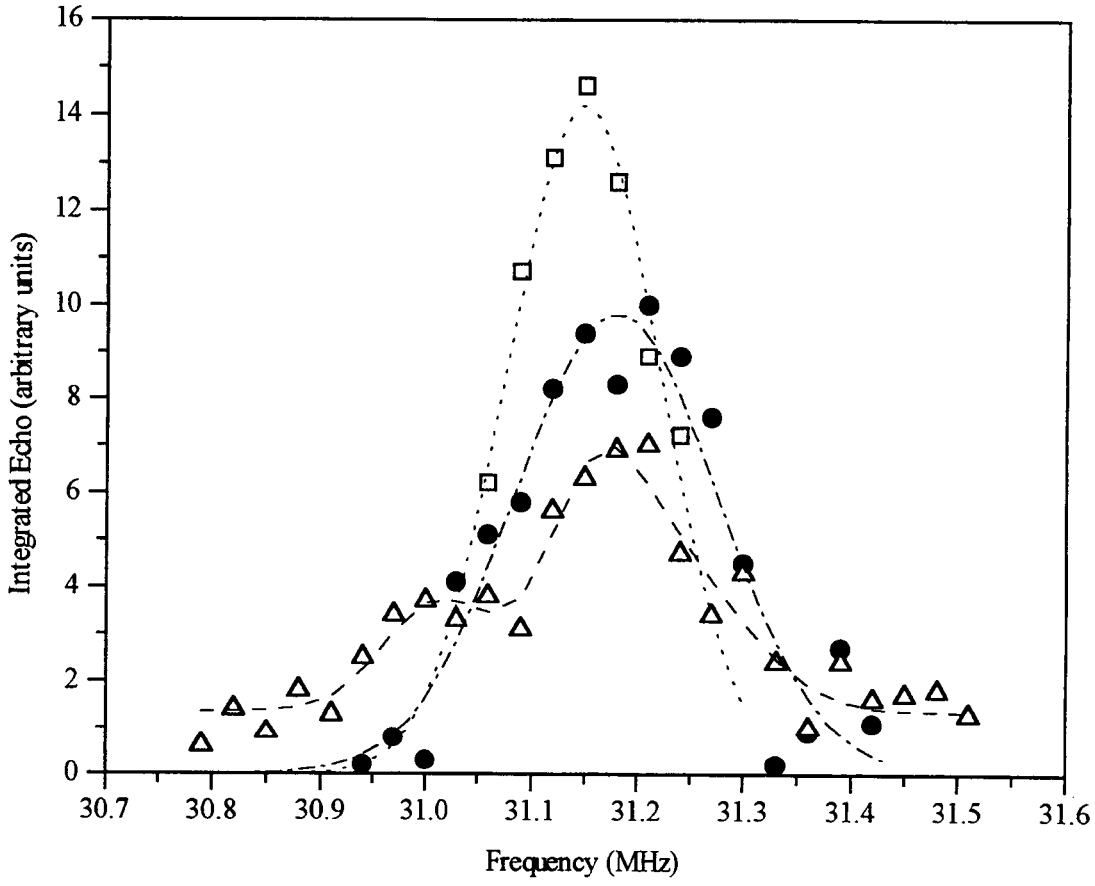

Figure 5.1. Cu(2) room temperature NQR spectra. Squares denote the Reference sample; circles denote the Good sample; triangles denote the Poor-Oxygen sample. Lines are a guide for the eye.

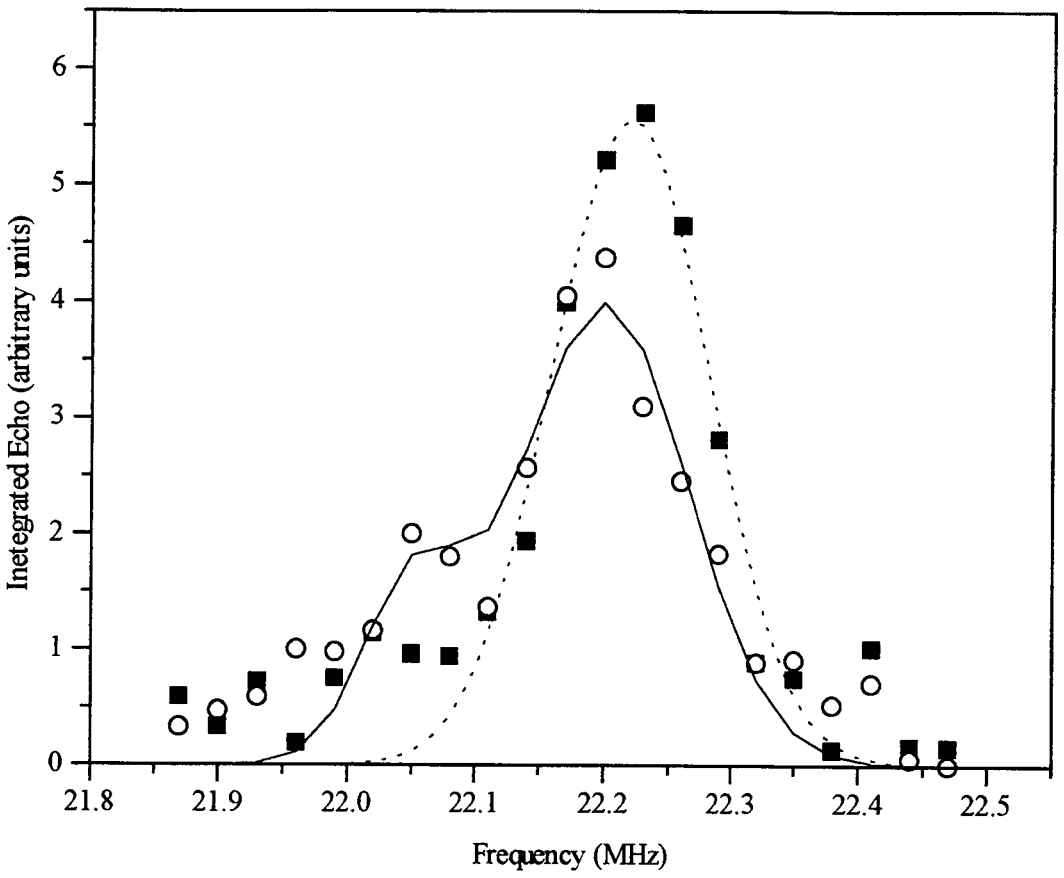

Figure 5.2. Cu(1) room temperature NQR spectra. Closed points denote the Reference sample; open points denote the Good sample. Lines are a guide for the eye.

was examined for the Reference sample, the Good sample, and the Poor-Vacuum sample. (See Fig. 5.2)

Although the samples made by Dr. Sleight's group appeared the same when tested using X-ray diffraction and ac susceptability measurements, differences could be detected using NQR. Looking at the Cu(2) site, the height and width of the NQR signal varied from sample to sample, with the NQR lines of all samples being smaller and broader than that of the reference sample. Both Poor samples were nearly identical, showing a shoulder

on the low frequency side of the spectrum. At the Cu(1) site, both the Good and Poor-Vacuum samples exhibited a significant shoulder on the low frequency side of the specrum when compared to the reference sample. A smaller NQR signal suggests that the sample is slightly oxygen deficient. (See Sec. 3.1) At a later point in time, the material was examined with X-ray microprobe, which revealed slight differences in oxygen content in the different grains. The shoulder on the Poor samples is indicative of some disorder in the sample. An example of disorder would be an oxygen atom or a cation at a wrong site. The Fair sample (not shown) had a Cu(2) NQR signal that was comparable in size to the Poor sample signal, but without an obvious shoulder.

The reason NQR can distinguish between similar samples when other characterization techniques do not is that NQR is very sensitive to differences in the local environment of a probe atom. By looking at a given frequency range, only atoms with the environment that corresponds to that range will be seen. In this experiment, I only looked at Cu sites in fully oxygenated material. A slight decrease in oxygen content creates a significant decrease in the intensity of the NQR signal. (See Sec. 3.1) Minor disorder that does not show up in X-ray diffraction will also decrease the NQR signal.

5.2 Effect of Heating on Samples' NQR Signal at Room Temperature

Although the NQR signal was expected to decrease at higher temperatures, the effect of heating on the room temperature spectra was unknown. If the sample was damaged at elevated temperatures, further experimental runs and analysis on the same

sample would have to take this into account. To determine the effects of heating, the Cu(2) spectra immediately before and after heating to 200°C were compared.

For the Good sample, the NQR signal recovered completely after heating. The other samples however did change upon heating. (See Fig. 5.3) After heating the Poor-Oxygen sample, the room temperature NQR signal had decreased by ~30%. However, when the sample was reheated, no further changes were seen. A possible cause for this change in the signal is a re-annealing of the sample.

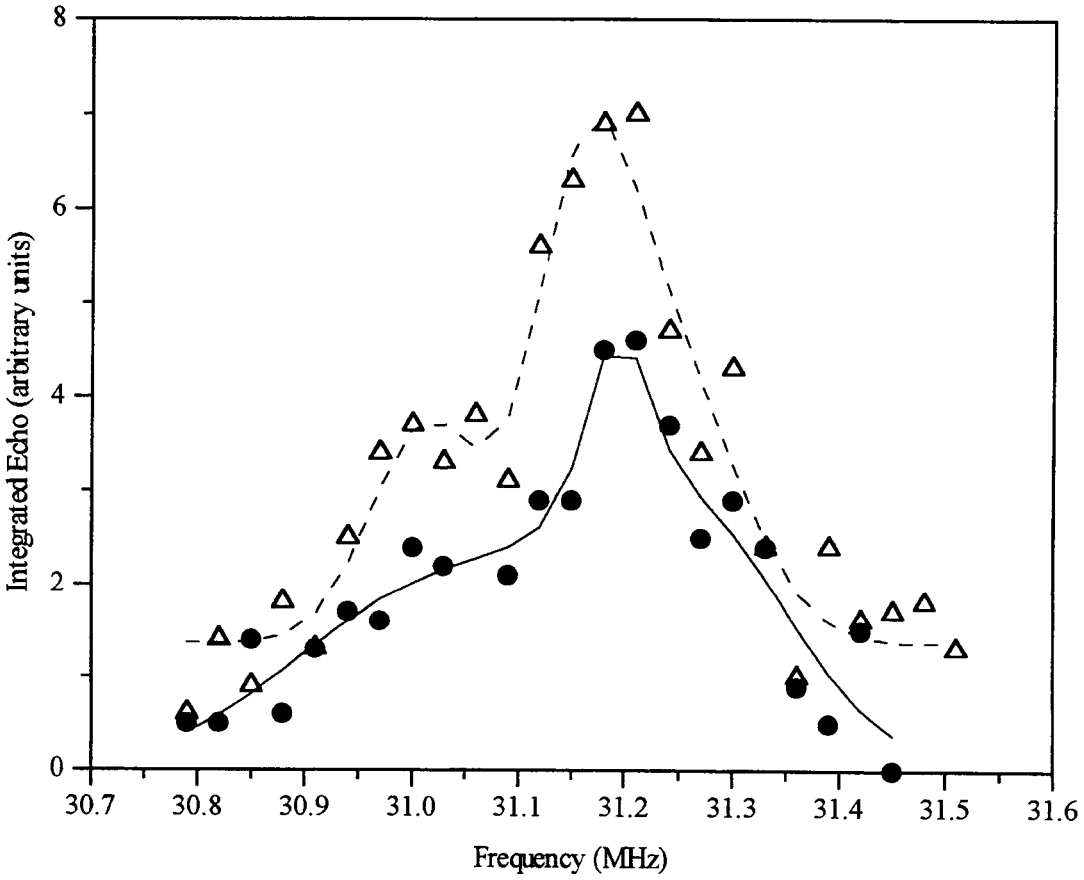

Figure 5.3. Cu(2) room temperature NQR spectra of Poor-Oxygen sample. Open points denote the sample before heating; closed points denote the sample after heating. The lines are a guide for the eye.

5.3 Effect of Elevated Temperatures on Signal Intensity

By the Curie Law (See Sec. 2.3.1), the signal intensity multiplied by the temperature should be a constant. By plotting this value against temperature, a clearer picture of what is happening to the signal intensity at higher temperatures is possible. Of course, this assumes that the behavior of the spectrometer over the temperature range is constant. The ATT spectrometer shows no obvious temperature dependence. (See Sec. 4.1.1) For the NQR study, the central fifteen points, corresponding to a frequency range of 0.42 MHz, were integrated. Fewer points were used if the signal was present for a smaller frequency range.

5.3.1 The effect of elevated temperatures on the NQR signal

Looking at the Good sample, it is obvious that the NQR signals at both the Cu(1) site and Cu(2) site do not follow the Curie law. (See Fig. 5.4) Looking at the Cu(2) site, the NQR signal follows the Curie law up to about 125°C, at which point, the signal intensity drops off rapidly and is gone at 200°C. When Poor-Oxygen was tested, the Cu(2) signal disappeared at 150°C and exhibited no sign of Curie-like behavior. (See Fig. 5.5) The Fair sample showed a similar behavior. Examining the Fair sample below room temperature, it was found that it exhibited a Curie-like behavior below -50°C. (See Fig. 5.6)

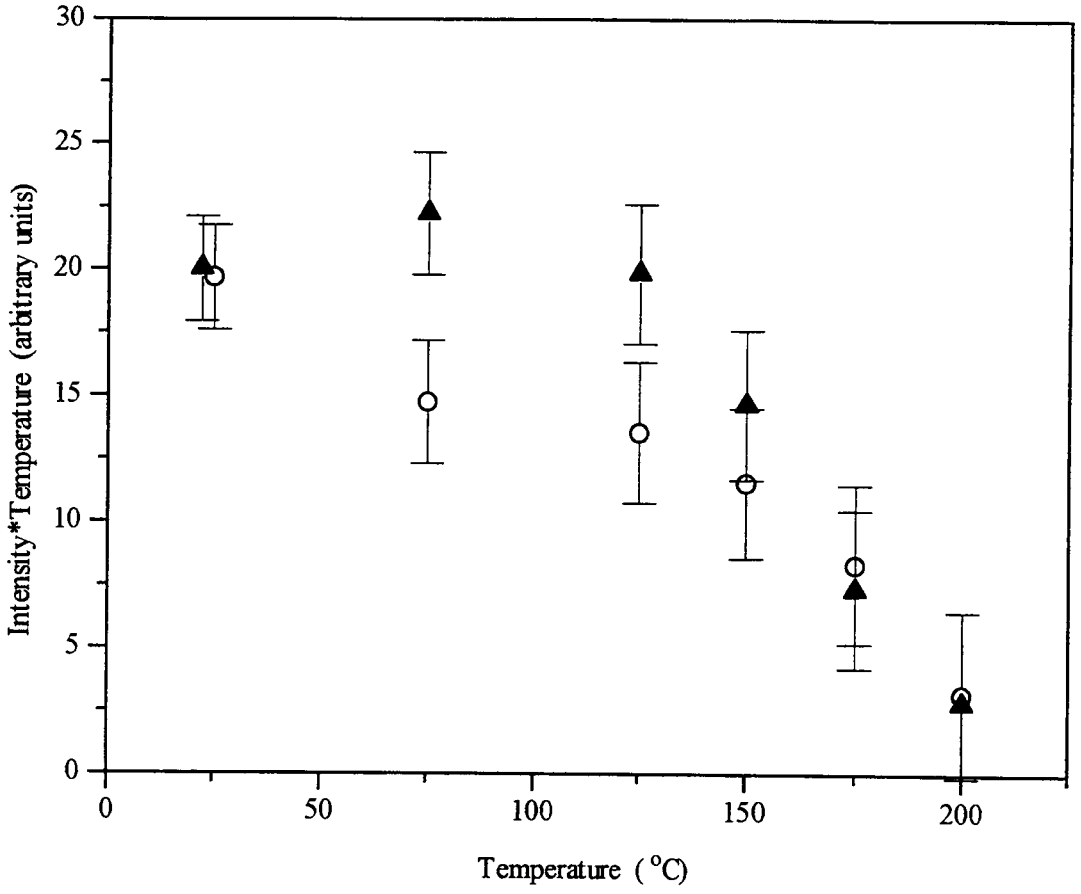

Figure 5.4. NQR signal intensity's dependence on temperature for the Good sample. Open points denote Cu(2); closed points denote Cu(1).

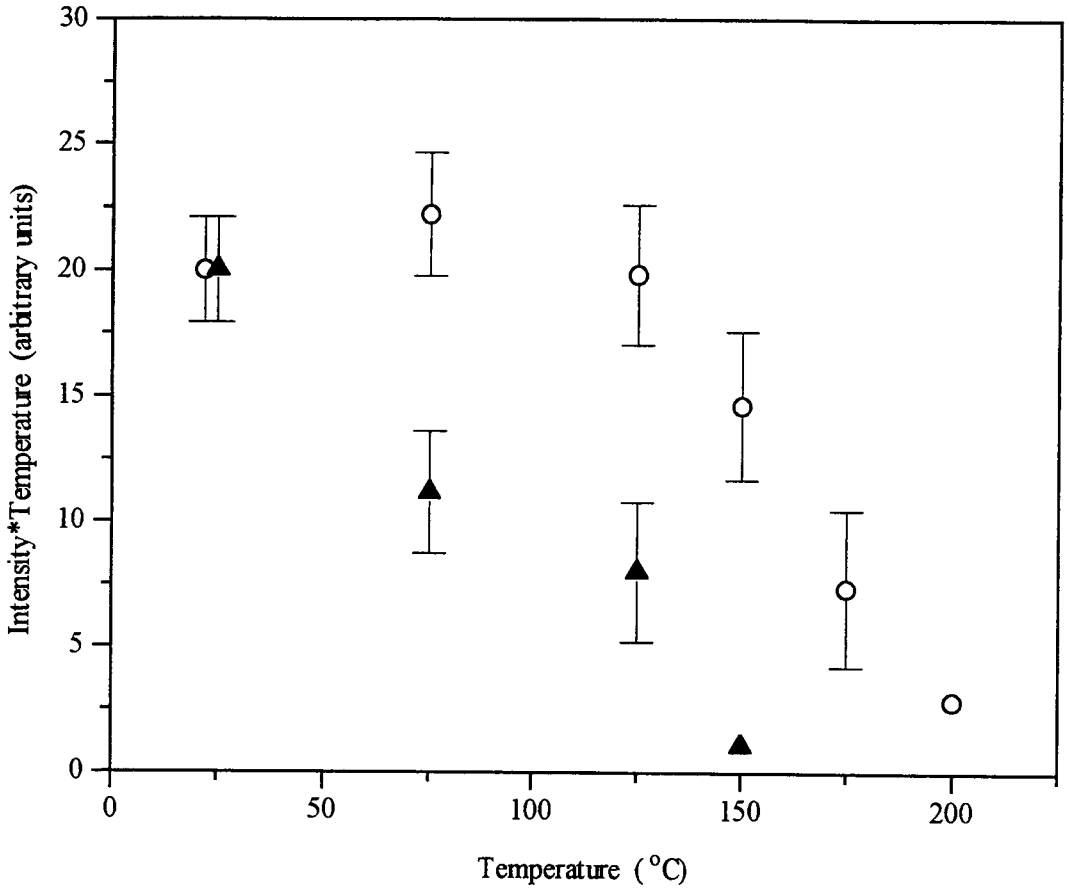

Figure 5.5. Cu(2) NQR signal intensity's dependence on temperature for samples of different quality. Open points denote the Good sample; closed points denote the Poor-Oxygen sample.

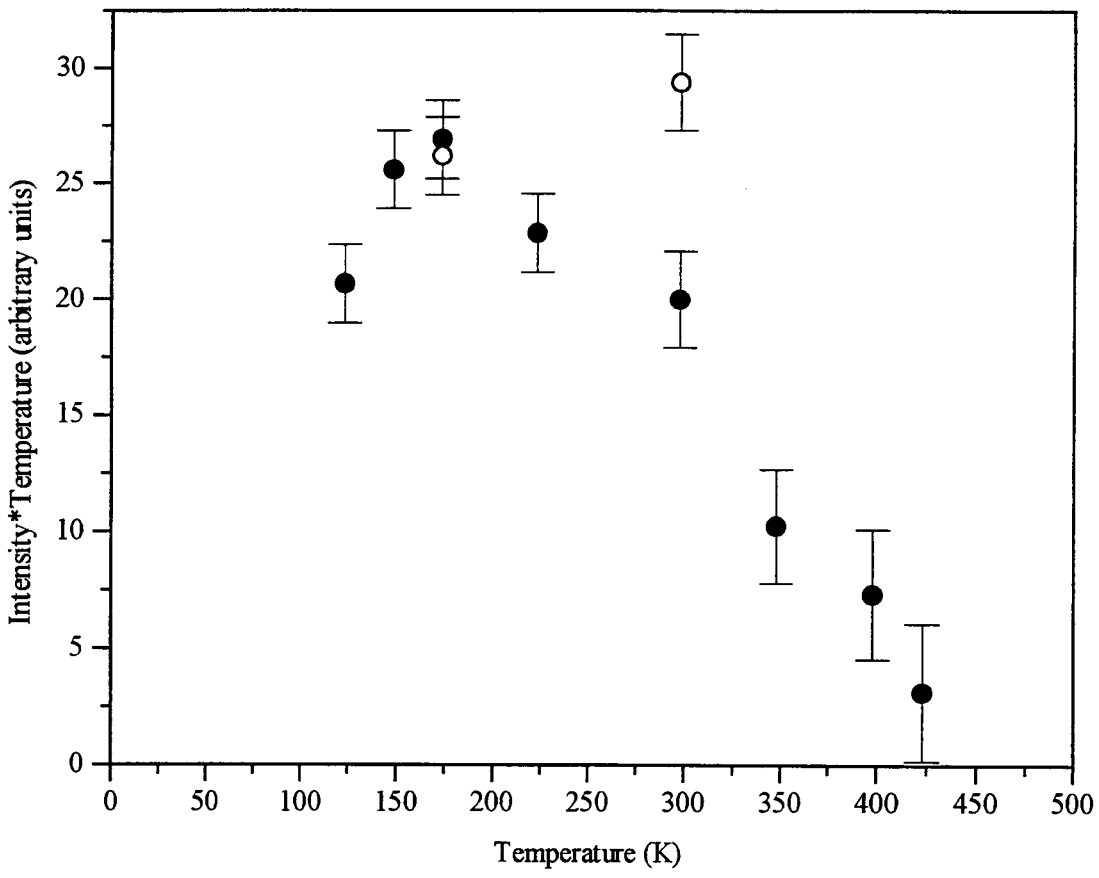

Figure 5.6. Cu(2) NQR signal intensity's dependence on temperature for the Fair sample. Open points denote Reference sample, which was scaled for ease of comparison.

Althought the T_1 behavior of the Cu(2) site is close to being constant throughout the temperature range examined, the T_1 for the Cu(1) site is not, with T_1^{-1} increasing with increasing temperature. This creates problems when data analysis is attempted over a range of temperatures for the Cu(1) site. It is obvious that the signal loss of both the Cu(1) and Cu(2) sites happen at the same temperature. This is not unexpected, because changes at the Cu(1) site will influence the Cu(2) site through changes in the bonds and the lattice parameters. Another difficulty associated with the Cu(1) site was the presence

of the shoulder on the low frequency side of the peak. Although this shoulder was included in the temperature analysis, it was difficult to determine if its behavior was the same as the main peak. For these reasons, it was decided not to continue the studies at the Cu(1) study, but instead to focus on the Cu(2) site.

Although oxygen diffusion into and out of the sample was not expected at these temperatures, a comparison was made between Poor-Oxygen, sealed in 1 atm of oxygen, and Poor-Vacuum, which was sealed in 10^{-5} Torr vacuum. (See Fig. 5.7) Both samples

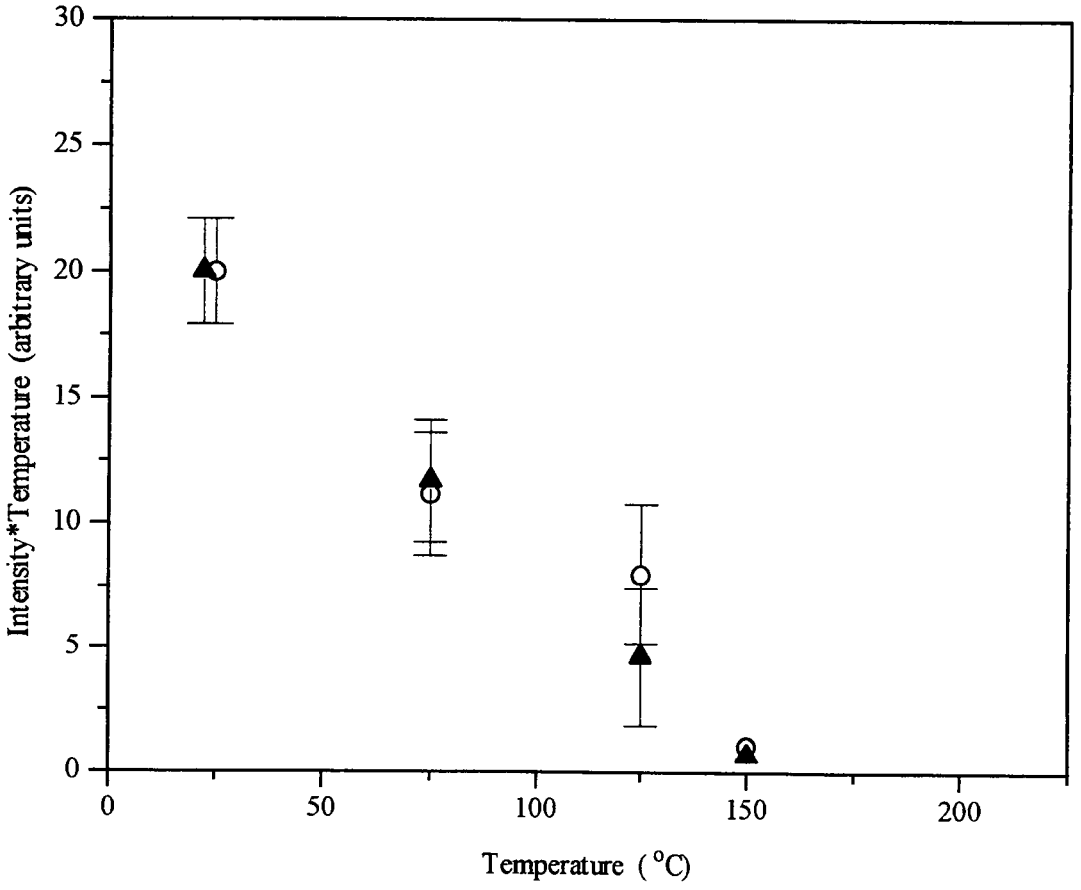

Figure 5.7. Cu(2) NQR signal intensity's dependence on temperature for samples sealed under different conditions. Closed points denote the Poor-Vacuum sample; open points denote the Poor-Oxygen sample.

had nearly identical room temperature NQR spectra after heating. Both samples exhibited the same behavior at higher temperatures, indicating that oxygen diffusion out of the samples was not the cause of the large decrease in signal intensity.

The resonance frequencies of the Cu(1) and Cu(2) sites above room temperature were compatible with previously published below-room temperature data. (See Fig. 5.8 and 5.9) When the line shape was examined, there was no obvious change in the full width at half maximum (FWHM) or in the line shape itself at the Cu(2) site. (See Fig. 5.10 and 5.11) The Cu(1) line shape was more difficult to analyze due to the shoulder on

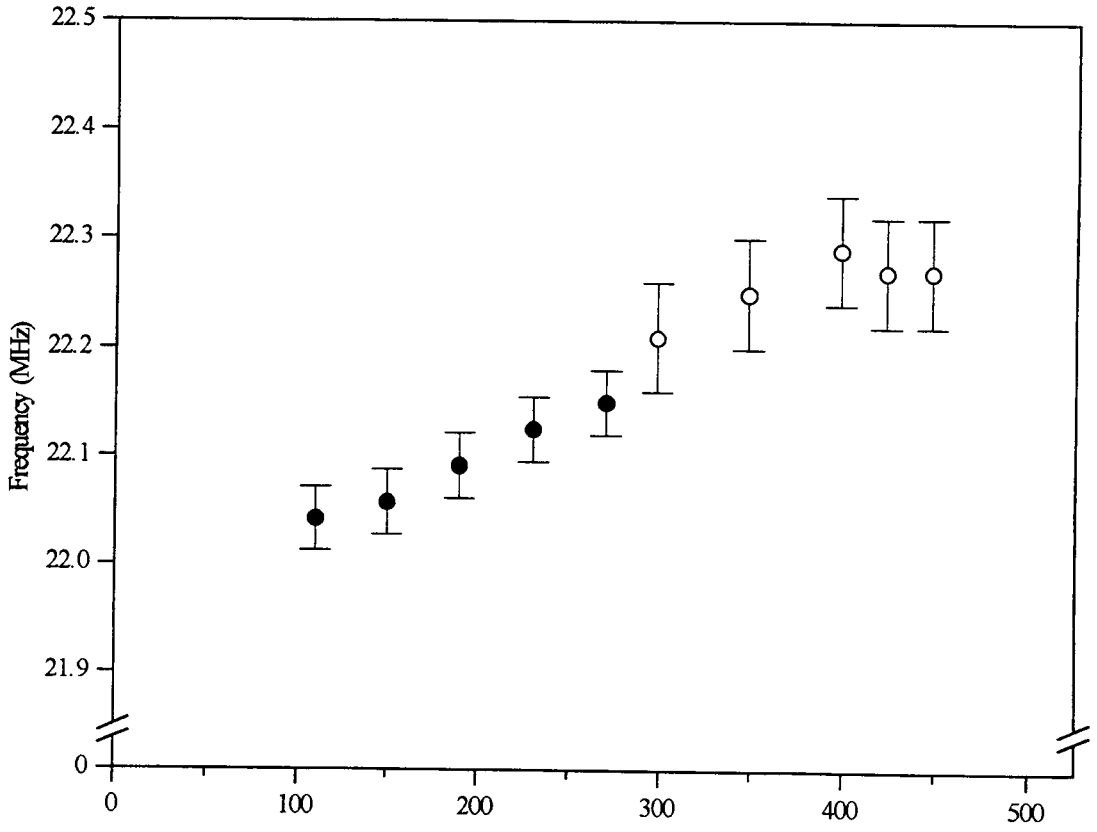

Figure 5.8. Temperature dependence of Cu(1) NQR frequencies. Open points denote the Good sample data; closed points are from ref. (12).

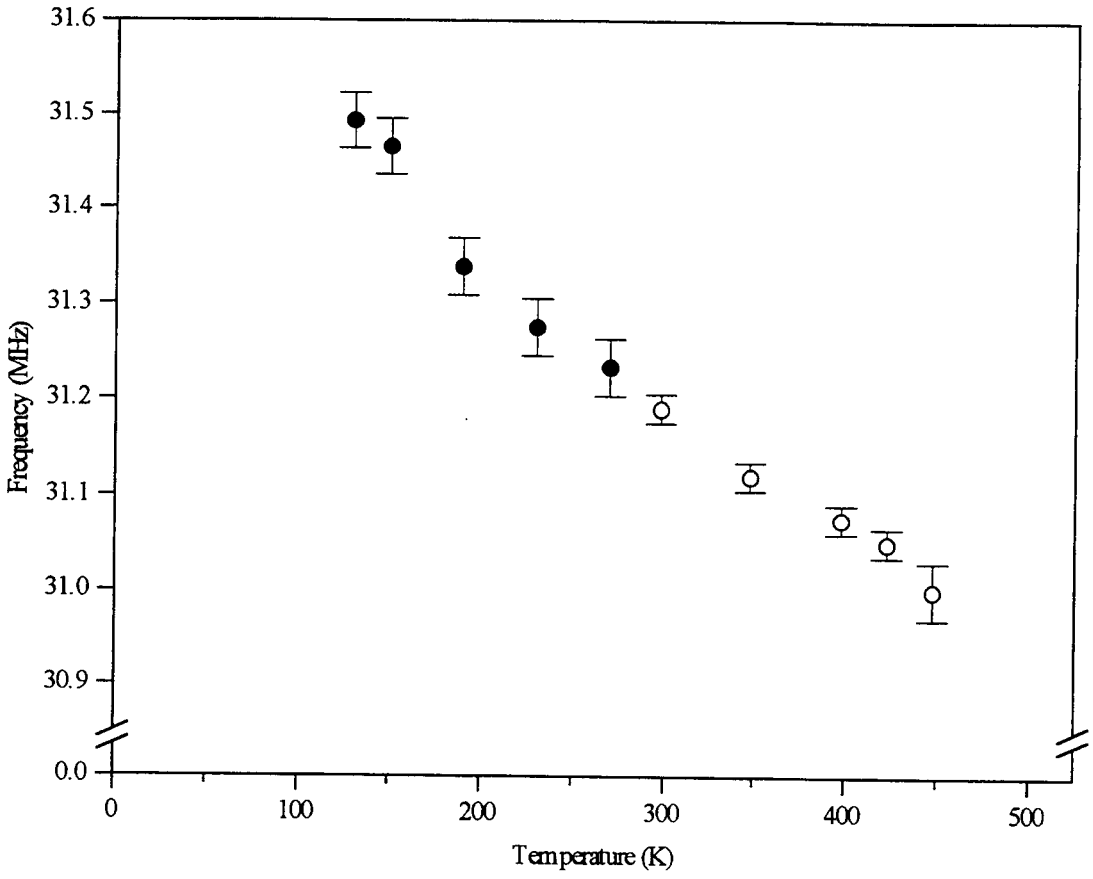

Figure 5.9. Temperature dependence of Cu(2) NQR frequencies. Open points denote the Good sample data; closed points are from ref. (12).

the peak, but it did not appear to significantly change with temperature. The NQR Cu(1) 31MHz signal with a long T_1 associated with the two-fold co-ordinated Cu(1) site was searched for, although it is associated with material that is far more oxygen deficient. As expected, there was no evidence of this signal being present.

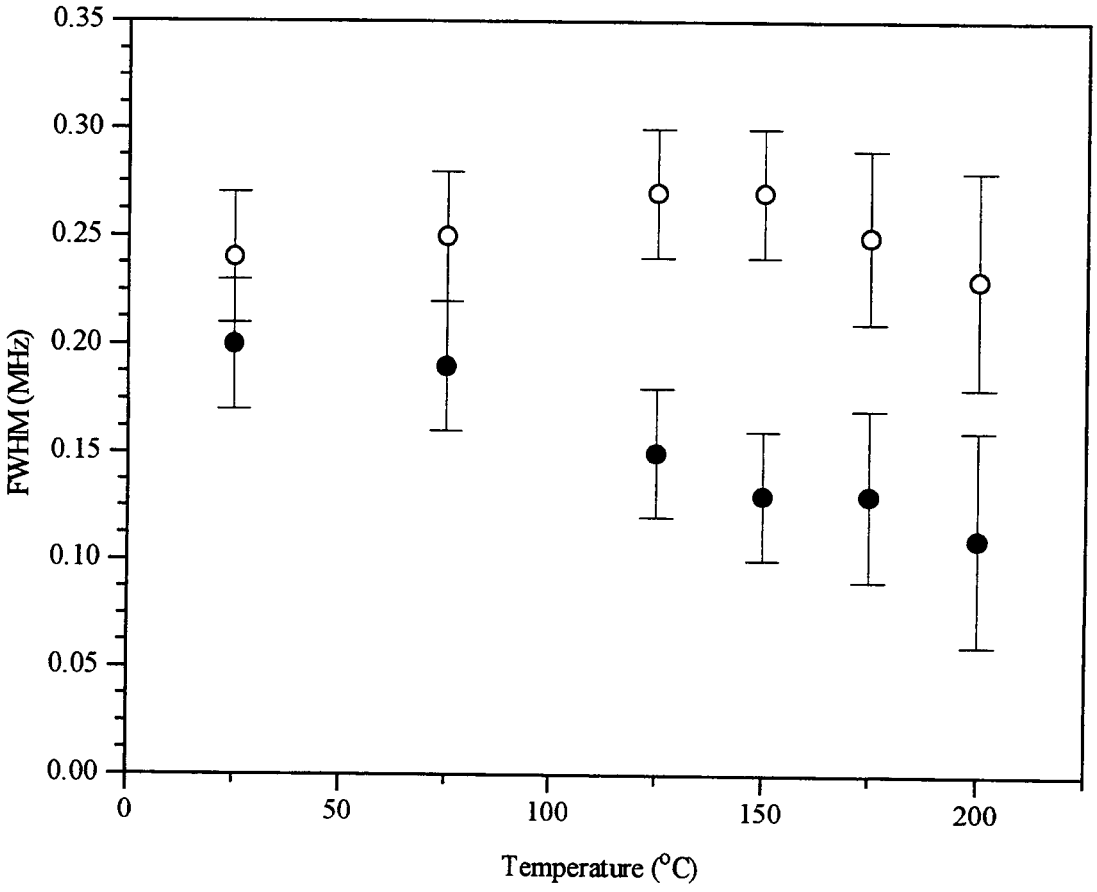

Figure 5.10. NQR temperature dependence of full width at half maximum for the Good sample. Closed points denote Cu(1); open points denote Cu(2).

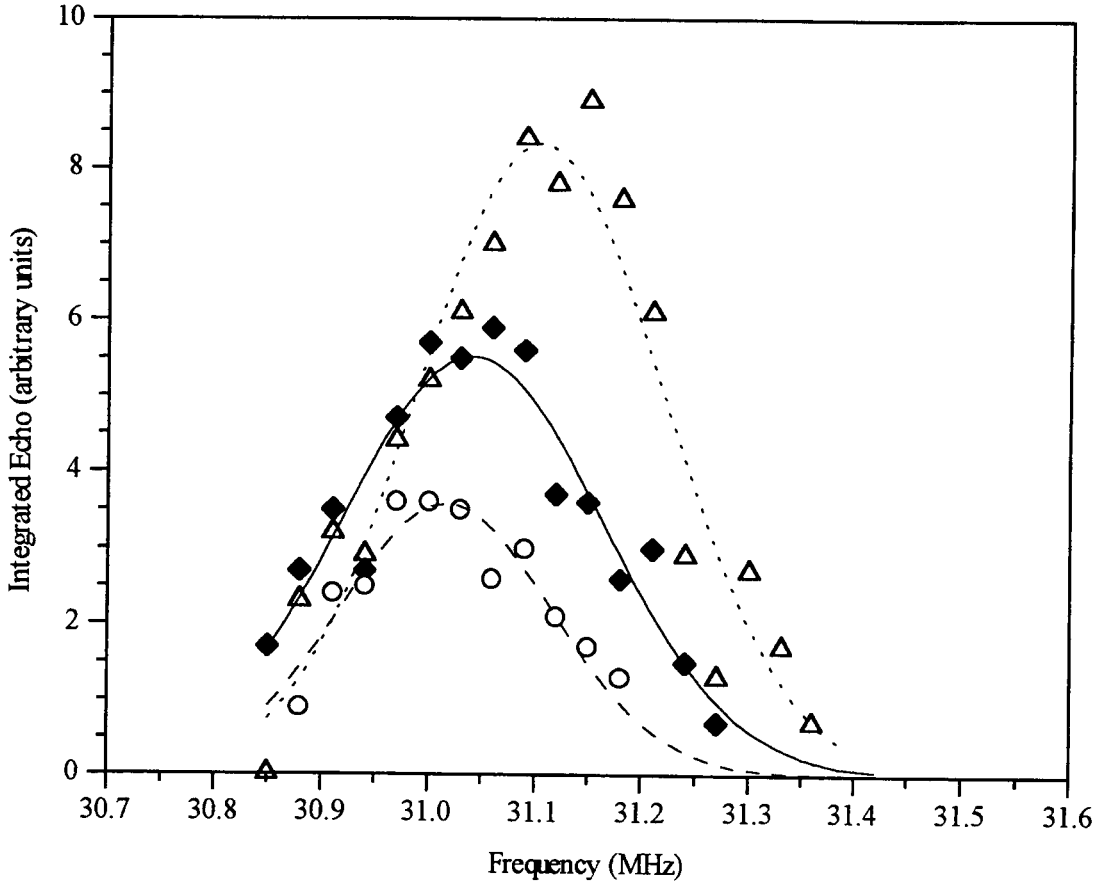

Figure 5.11. Temperature dependence of Cu(2) NQR line shape for the Good sample. Trianges denote 75°C; diamonds denote 150°C; circles denote 175°C. Lines are a guide for the eye.

5.3.2 The effect of elevated temperatures on the NMR signal

NMR was used to get a slightly different perspective on the disappearance of the NQR signal. The behavior of the NMR Cu(2) quadrupolar satellite is expected to directly correspond to the Cu(2) NQR signal. (See Sec. 2.5.2)

The first sample examined was the Oriented sample. The main spectrum, which includes the spin 1/2 transitions and the Cu(1) spin 3/2 transition, was measured for the

randomly oriented powdered material. (See Fig. 5.12) When heated up to 200°C, the main spectrum showed no noticable changes. Sample Oriented was then oriented in epoxy. (See Sec. 4.4) Although most of the sample did orient with the c-axis parallel to the magnetic field, there was an unexplained decrease of the overall signal intensity. As this epoxy had not been used before with $YBa_2Cu_3O_7$, it is possible that it was the source of the problem. Measurements of the main spectrum were then done on the material when it was oriented with the c-axis parallel to the magnetic field and with the c-axis

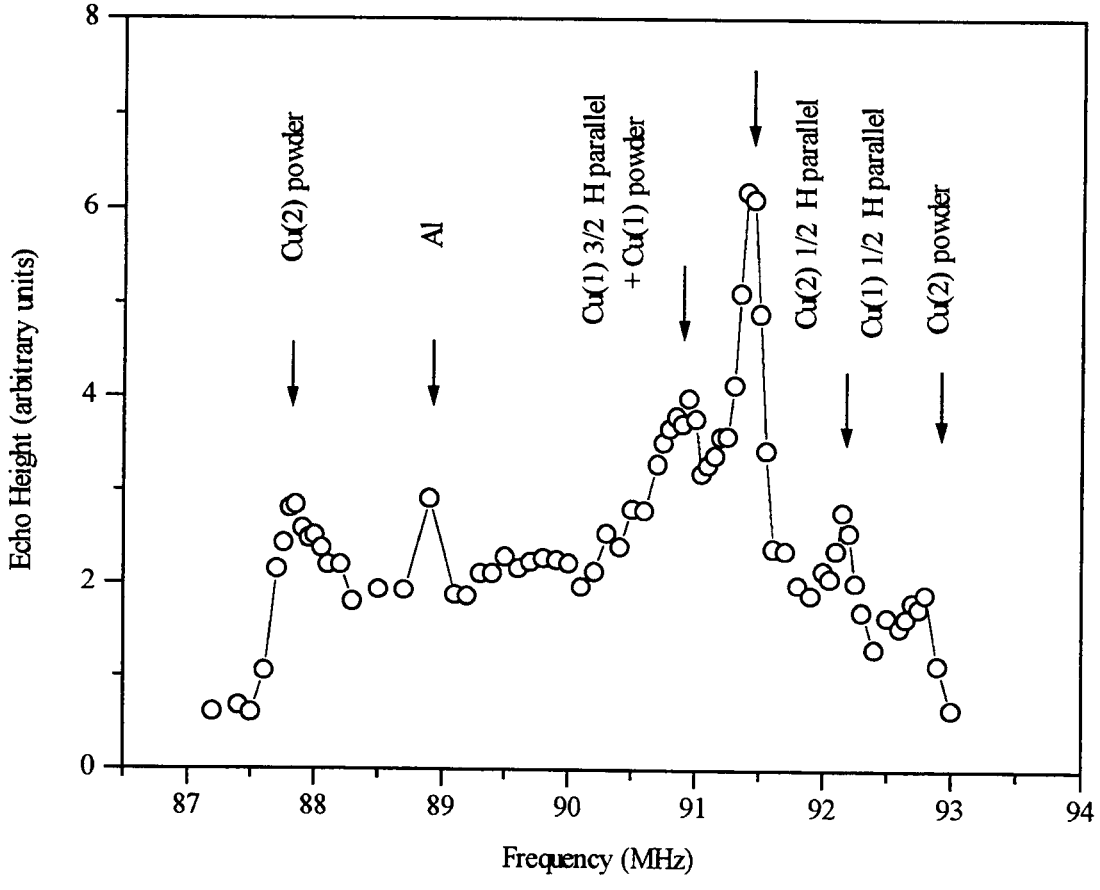

Figure 5.12 NMR room temperature powder spectrum for the Oriented sample.

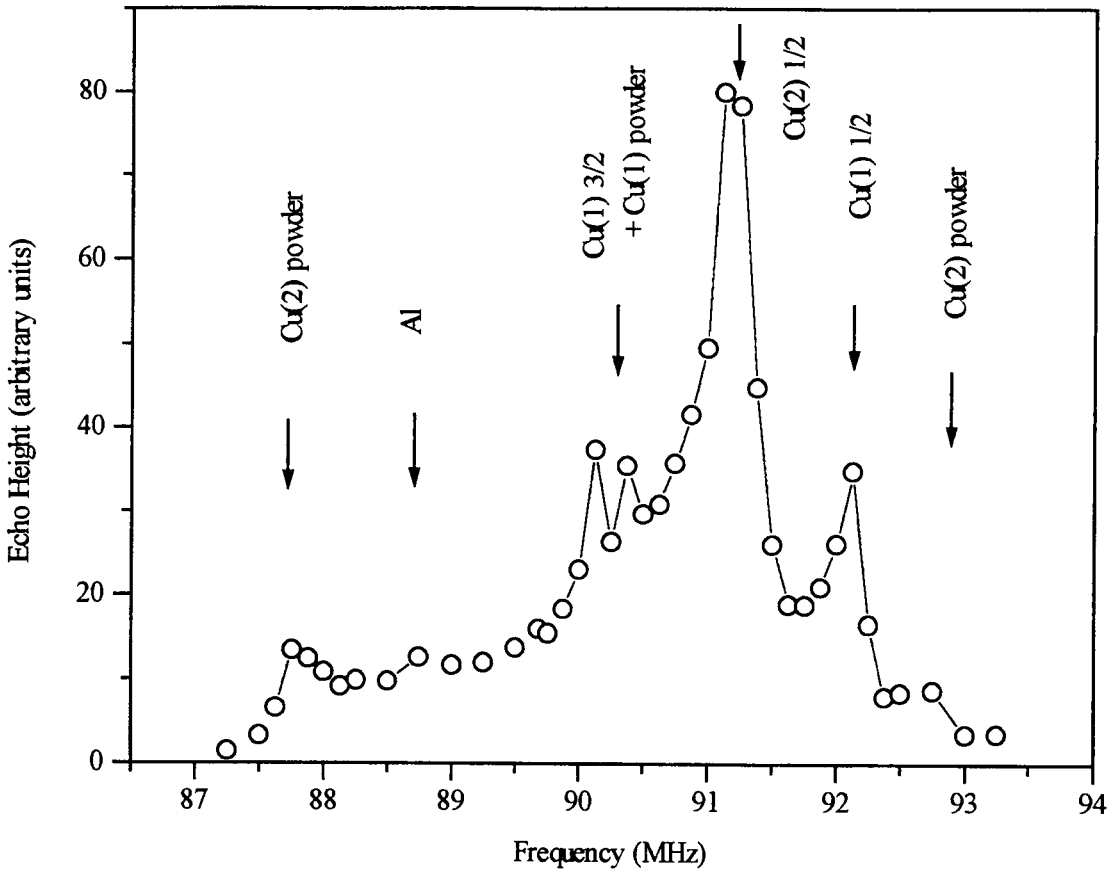

Figure 5.13. NMR room temperature spectrum for the Oriented sample oriented with the c-axis parallel to H_0.

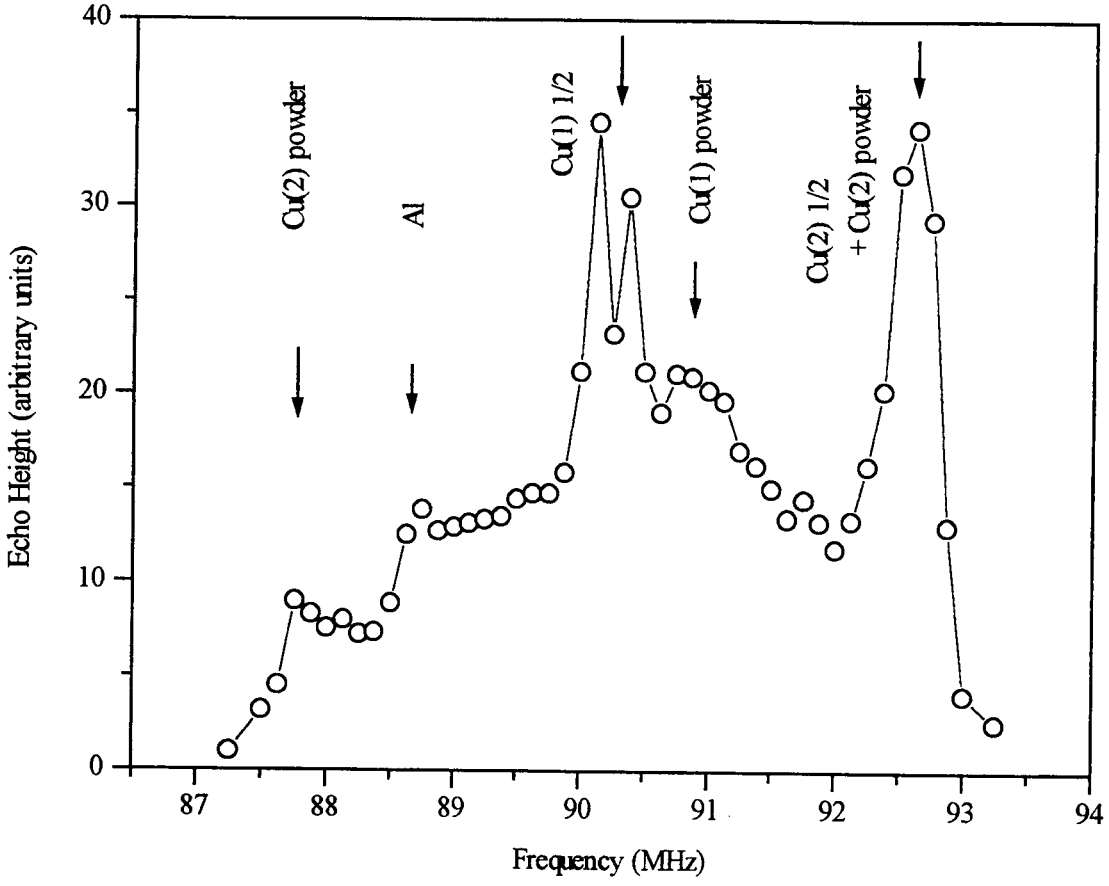

Figure 5.14. NMR room temperature spectrum for the Oriented sample oriented with the c-axis perpendicular to H_0.

perpendicular to the magnetic field. (See Fig. 5.13 and 5.14) Again, when the material was heated, it showed no change with temperature for either orientation.

Because of the unexplained problems with the epoxy, a new powdered sample, Fair, was used to examine the Cu(2) quadrupolar satellites. Because the material would partially align without epoxy, it was possible to measure the Cu(2) quadrupolar satellite associated with the c-axis parallel to the magnetic field. (See Fig. 5.15) However, the amount of material that was oriented would change if the NMR probe and the sample

were disturbed, which required that all tests be run in a single session. The main spectrum was again examined at 200°C, with no change being detected. The Cu(2) quadrupolar satellite was then examined, integrating the peak over a range of 0.8 MHz. (See Fig. 5.16) The behavior of the intensity of the signal was the same as that seen using NQR, as expected. As in NQR, the shape of the satellite did not change, nor did it show any unexpected frequency dependence on the temperature. The frequency range between the main spectrum and the Cu(2) satellite was examined at 150°C to determine if another

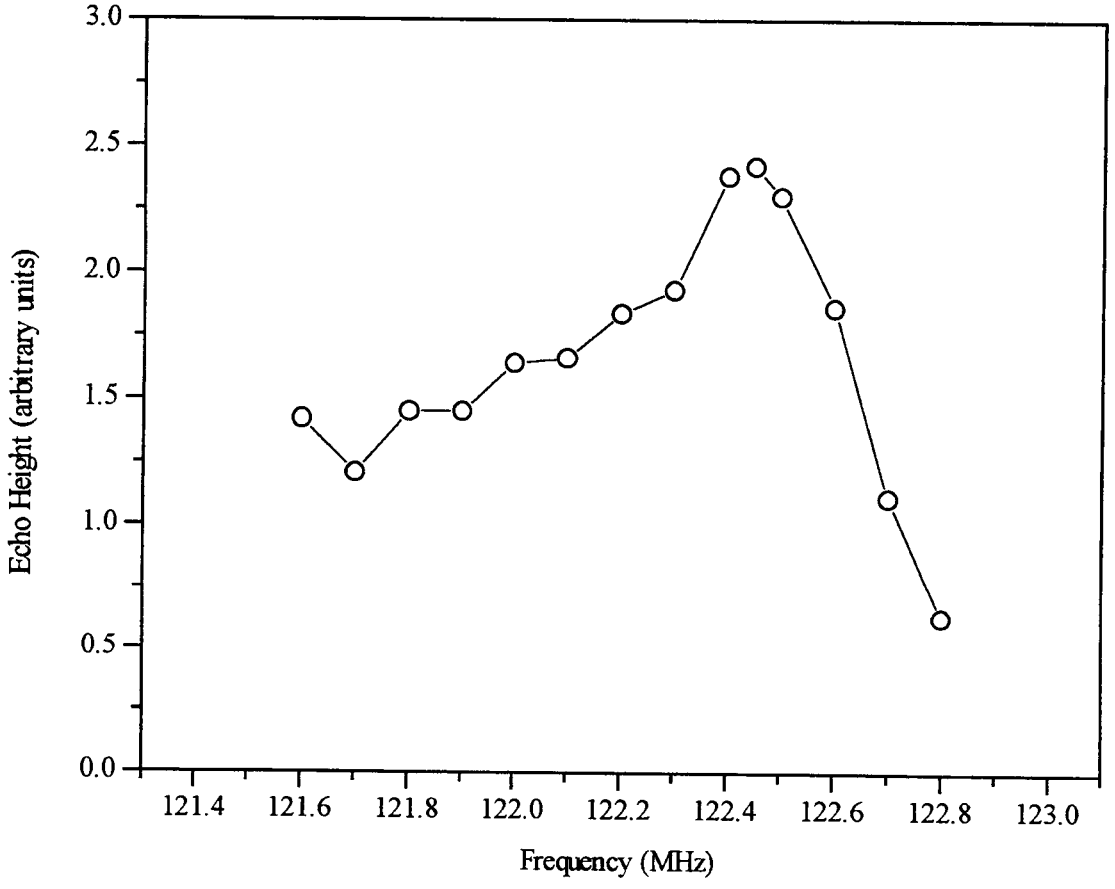

Figure 5.15. NMR room temperature Cu(2) quadrupolar satellite for the Fair sample.

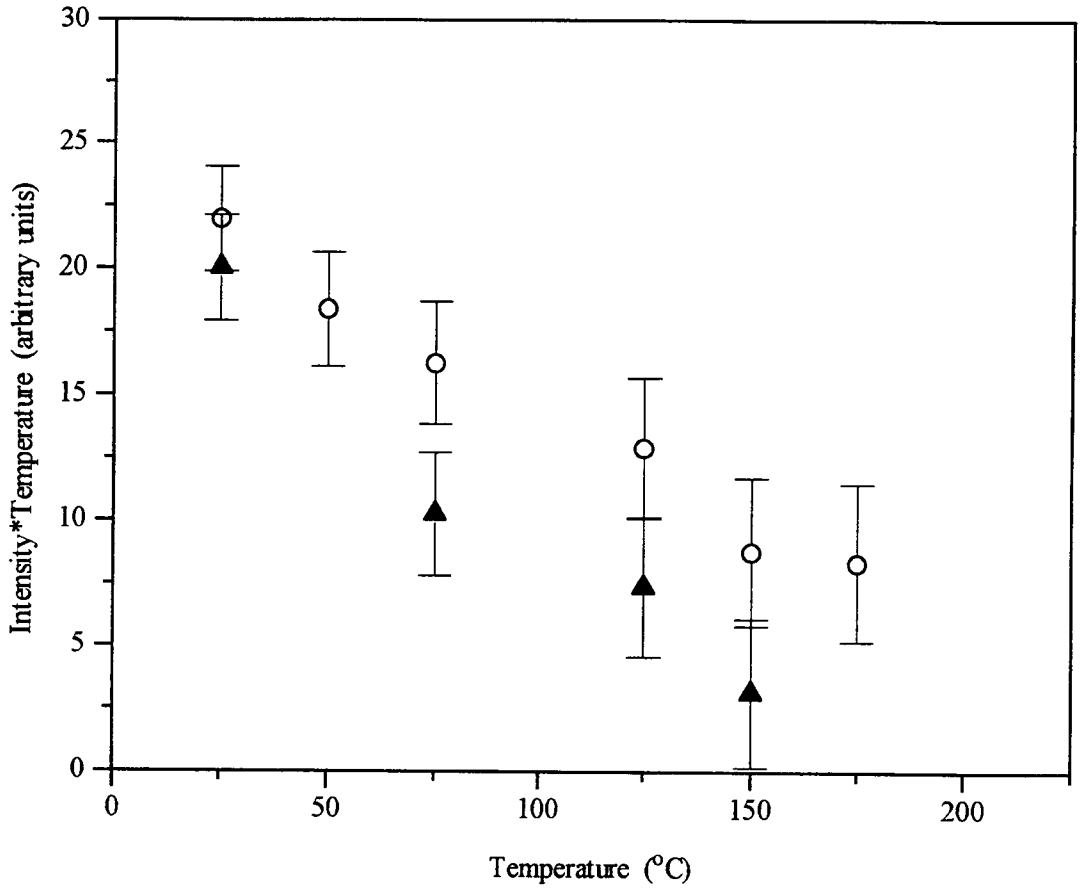

Figure 5.16. Cu(2) signal intensity's dependence on temperature for the Fair sample. Closed points denote NQR; open points denote NMR.

signal appeared when the quadrupolar satellite dissappeared. No new signal was detected in that frequency range, although it is possible that a signal could occur outside of that range.

5.4 T_2 Studies

Because I was looking at spin echoes, the intensity of the signal had a dependence on the T_2 of the material. In the following discussion and analysis of the T_2 data, all raw

data was scaled to the Curie Law by multiplying it by the temperature. There were two possibilities for how the signal was decreasing with temperature. If the extrapolated true intensity, I(0), of the signal at $2\tau = 0\mu s$ remains the same regardless of temperature, the signal intensity could be lower for larger τ values because of a T_2^{-1} value which was larger than expected. The second possibility was that the true intensity I(0) was lower at elevated temperatures. To determine the answer to this question, a T_2 study was performed on the Fair sample at several temperatures. (See Fig. 5.17)

The theoretical curves are calculated from the equation

$$I(t) = I(0)\exp\left(-\frac{t}{T_{2L}} - 0.5 \times \frac{t^2}{T_{2G}^{\ 2}}\right) \qquad \text{(Eqn. 5.1)}$$

where the lorentzian component is $T_{2L}^{\ -1} = 3.7T_1^{-1}$ for the Cu(2) site. (See Sec. 3.1) The values for T_1 were obtained by extrapolation of data previously published by Pennington *et al.*.[10] The gaussian component T_{2G} is dependent on the H_1 of the coil. Because the material appeared to be Curie-like at -100°C, I fit the data at that temperature to obtain T_{2G} and I(0). Assuming the temperature dependence of T_{2G} is not dependent on H_1, I used Itoh's T_{2G} temperature dependent data to extrapolate my values of T_{2G}. The values used are given in Table 5.1.

Comparing my data to the theoretical curves, it can be seen that the -100°C and 25°C data agree with the expected values. However, there is a significant difference at 75°C. There is an additional lorentzian component, $T_{2Extra}^{\ -1} = 0.0063\mu s^{-1}$, at 75°C. The data at all temperatures extrapolate back to the same true intensity value I(0). This implies that the decrease in the signal intensity is being caused by a T_2 process.

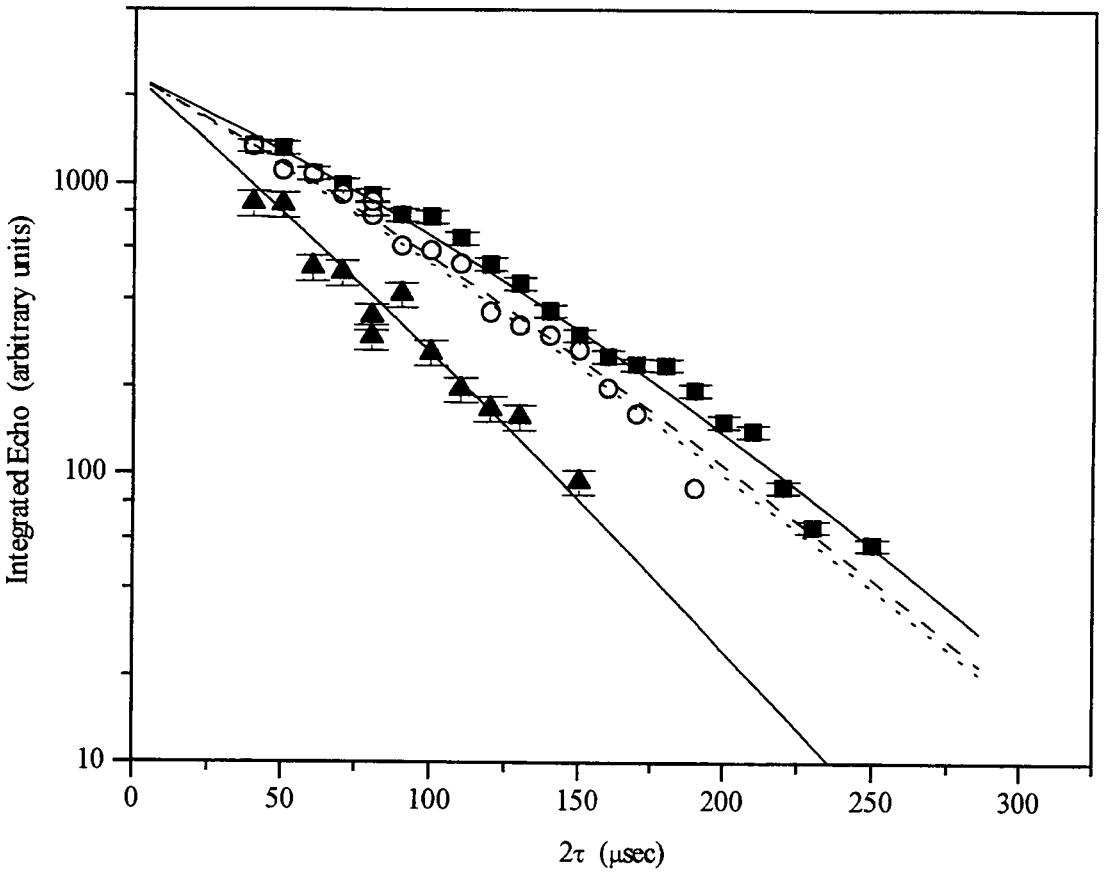

Figure 5.17. NQR Cu(2) T_2 study of the Fair sample. Closed circles denote -100°C; open circles denote 25°C; triangles denote 75°C. The lines are theoretical T_2 curves. The upper solid line denotes -100°C; the dashed line denotes 25°C; the dotted line denotes 75°C. The lower solid line is a fit to the 75°C data.

Because the additional lorentzian T_2 appears to be thermally activated, presumably it is the rate of the fluctuation of the electric field gradient. Setting $T_{2Extra}^{-1} = \tau^{-1}$, it should be possible to obtain an attempt frequency and activation energy for the process that is occurring. (See Fig. 5.18) Unfortunately a standard T_2 study is extremely difficult to perform at higher temperatures because of the loss of signal intensity expected by the Curie Law, the loss due to T_{2Extra}, and the increased amount of thermal noise. To obtain

Table 5.1. T_2 values

TEMPERATURE (°C)	T_{2L}^{-1} (μs^{-1})	T_{2G}^{-1} (μs^{-1})
-100	0.0111	0.00549
25	0.0132	0.00465
75	0.0139	0.00435
125	0.0146	
150	0.0150	
175	0.0151	
200	0.0153	

points for temperatures above 75°C , the intensity data was scaled. For the Fair sample, this was done by scaling the room temperature intensity to equal the echo height. For the Good sample, the data was known to be Curie-like at room temperature. This value, corrected for T_2, was then used as I(0). The higher temperature data was then corrected for the expected T_2 component. The remaining decrease of the signal with temperature was then assumed to be from T_{2Extra}.

The activation energy for the Fair sample was found to be $E = 0.21 \pm 0.04eV$. The attempt frequency was $\tau_0^{-1} = 7 \pm 2 \times 10^6 s^{-1}$. The activation energy of the Good sample was $E = 0.64 \pm 0.04eV$. The attempt frequency was $\tau_0^{-1} \approx 10^{11} s^{-1}$.

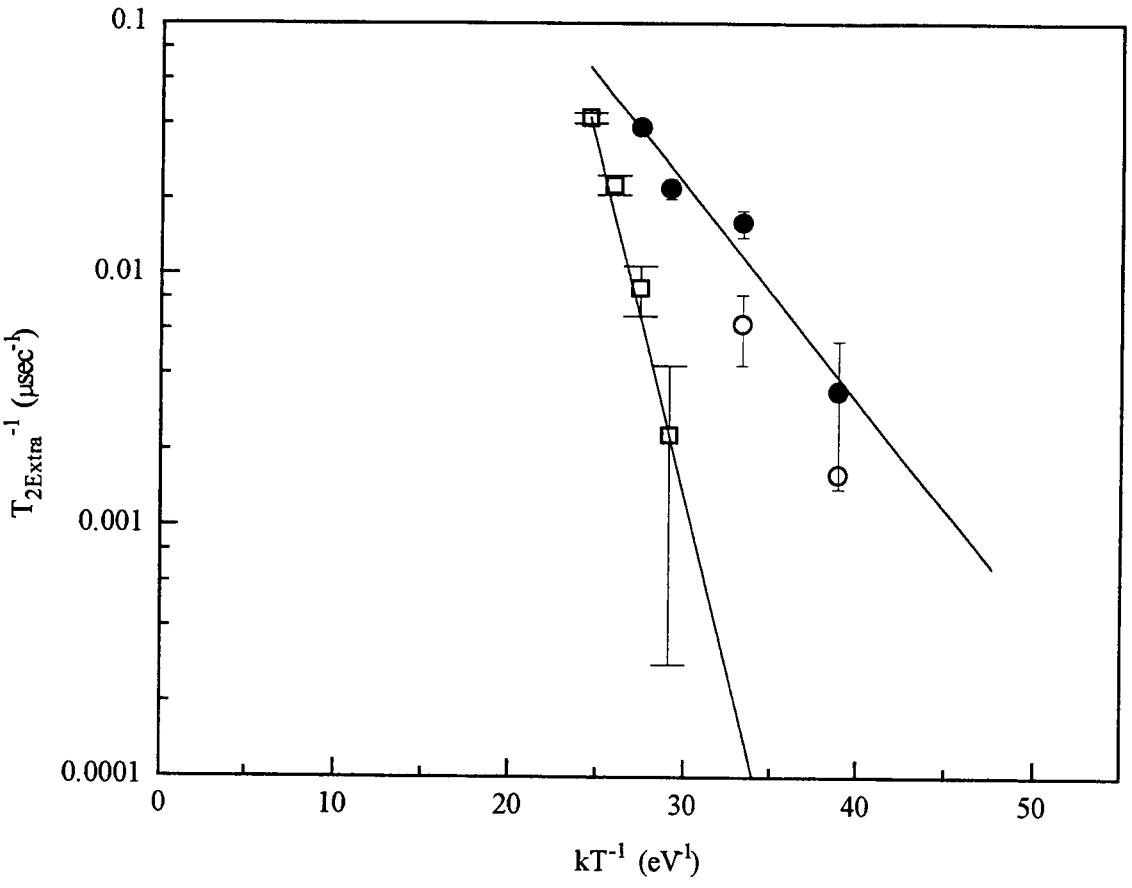

Figure 5.18. Arrhenius plot of the extra T_2 component of the Cu(2) NQR signal. Closed circles are from the Fair sample's intensity data; open circles are from the Fair samples T_2 data. The Fair sample's fit uses $T_{2Extra} = 8.6\exp(-0.2/kT)$. Open squares are from the Good sample's intensity data. The Good sample's fit uses $T_{2Extra}^{-1} = 2\times10^{5}\exp(-0.64/kT)$.

6. DISCUSSION

Both Cu NQR and NMR quadrupolar satellite transitions exhibited a non-Curie like loss of signal intensity near room temperature. However, at low enough temperatures, Curie-like behavior is exhibited at the Cu sites.

The NQR results showed a dependence on the sample quality. The higher quality sample behaved Curie-like up to a higher temperature than the lower quality samples. The NQR signal in the higher quality sample also disappeared at a higher temperature compared to the lower quality samples. The difference in behavior between samples was not dependent on oxygen diffusion into or out of the sample, which eliminates a compositional change in the material at higher temperatures as a cause of the decrease in signal intensity.

The T_2 studies demonstrated that the loss of signal was caused by an additional attenuation of the spin echo. If a higher temperature created a fixed change in the structure due to the formation of new sites, a new frequency would be expected. This new frequency would decrease the true intensity, I(0), at the old frequency. As the T_2 studies show, there is no change in I(0), it is the behavior of T_2 that changes.. There was also no evidence of a new frequency showing up between the NMR main line and the quadrupolar satellite. This combined with the increase in T_2^{-1} suggests a fluctuating field gradient.

If the field gradient were to fluctuate fast enough, a new signal might appear. It would be caused by the Cu atom seeing an an average of the two electric field gradients. In order for this new signal to be seen, the jump rate τ^{-1} needs to be greater than the

difference between the frequencies of the two field gradients. Given that it appears that the fluctuating field gradient causes a significant change in the frequency, the jump rate would need to be of an order greater than ω_0, in this case $10^8 s^{-1}$. Trying to find this new signal is not practical because the frequency that it occurs would be unknown. In addition, at higher temperatures other motional processes will occur in the material.

The fluctuation of the field gradient is obviously triggered by an increase in temperature and is dependent on sample quality. The activation energy 0.2-0.64 eV is the same order of magnitude as activation energies found for the motion of oxygen. The Good sample has a slightly lower attempt frequency τ_0^{-1} and activation energy than that found in bulk oxygen diffusion. (See Sec. 2.2) However, for the Fair sample, the value τ_0^{-1} is much lower than expected for single atom motion induced by lattice vibrations, which are typically of order $10^{13} s^{-1}$.

A candidate for the cause of the fluctuation of the field gradient could be the motion of oxygen atoms in the chain layer. The oxygen atoms are the most mobile of the atoms in $YBa_2Cu_3O_7$. A hop of an oxygen atom from its regular O(1) site into an interstitial O(5) site would change the field gradient at the Cu(1) site. It is known that oxygen vacancies in the chain layer cause a significant shift in the Cu(2) frequencies. An oxygen in an interstitial position would be expected to cause a significant shift (several MHz) in the resonance frequency at the Cu(1) site. The field gradient at the Cu(2) site also would be influenced, not just by being a neighbor to the Cu(1) site, but by shifts in the Cu(2) position relative to its immediate oxygen neighbors caused by a change in the oxygen positions in the chain layer. The oxygen hops could be correlated, with the

oxygen not contributing to bulk diffusion at these temperatures but returning to its original or nearby O(1) site.

It is interesting to note that the more stable compound, $YBa_2Cu_4O_8$, has an NQR signal that is observable at much higher temperatures. The oxygen stoichiometry in that compound is far more stable, which discourages oxygen motion at lower temperatures.

The lower activation energy and low attempt rate in the Fair sample might be explainable by a dependence of the motion of the oxygen atoms on defects or vacancies. Theoretical calculations have shown that oxygen jumps in the chain layer are more likely if there is a nearby vacancy. (See Sec. 3.2.5) The higher quality sample has a higher activation energy than the lower quality sample, supporting the possibility that increased disorder encourages oxygen motion by lowering the energy barrier. Although the attempt frequency seen in the Good sample is typical of phonon induced atomic motion, the low attempt frequency seen in the Fair sample implies that there the attempt frequency is not dependent on the phonon vibrations alone.

Because the material appears to disappear at a uniform rate and all Cu(2) sites are affected, the factor that controls the jumping of the oxygen atoms is homogeneous. If each vacancy only effects nearest neighbor chain layer oxygens, one would expect a rather high level of oxygen vacancies would be necessary to observe the complete lack of signal seen at higher temperatures. However, as is evident from the room temperature spectra, a good portion of the material is not disordered or oxygen deficient. If disorder was required, a portion of the sample would not be expected to show oxygen motion at the temperatures studied. The portion of the sample which is perfect should be unaffected and

would obey the Curie law at higher temperatures. A reduced signal would then still be present at higher temperatures, which was not observed.

For the material to demonstrate such homogeneous behavior implies a correlation between the oxygen atoms which are jumping. It is possible that when one oxygen atom jumps, it lowers the energy barrier necessary for its nearest neighbors to jump. This would make it possible for a large number of oxygen atoms to jump in a short amount of time. The low attempt frequency would reflect the requirement that the oxygen atoms move together. For the material with fewer vacancies, the energy barriers would be higher and correlated oxygen motion would be more difficult. The only factor influencing the attempt frequency for oxygen motion would then be lattice vibrations.

7. CONCLUSION

The NQR and NMR studies of $YBa_2Cu_3O_7$ near room temperature have demonstrated an additional attenuation of the quadrupolar signal intensity at higher temperatures. The temperature at which this attenuation occurs varies according to sample quality, with lower quality samples showing attenuation at lower temperatures. The activation energy 0.2-0.64 eV is of the same order of magnitude as activation energies for oxygen motion found using other experimental techniques. However, in the lower quality sample, the attempt frequency $\sim 10^6\ s^{-1}$ is far lower than a simple phonon activated process, which suggests an additional controlling factor which may be dependent on oxygen vacancies in the chain layer. Short range hopping of the oxygen atoms in the chain layer is a likely candidate for the atomic motion which is observed.

BIBLIOGRAPHY

[1] J. Reyes-Gasga *et al.*, Physica C **159**, 831 (1989).

[2] B.W. Veal *et al.*, Phys. Rev. B **42**, 6305 (1990).

[3] J.D. Jorgensen *et al.*, Phys. Rev. B **36**, 3608 (1987).

[4] J.D. Jorgensen *et al.*, *Proceedings of the Workshop on Lattice Effects on High Temperature Superconductors*, Sante Fe, NM, 1992, Y. Bar-Yam *et al.*, ed. (World Scientific, Singapore, 1992).

[5] Laudise *et al.*, J. Crys. Growth **85**, 569 (1987).

[6] C.P. Slichter, *Principles of Magnetic Resonance*, 3rd ed. (Springer-Verlag, Berlin, 1990).

[7] A. Abragam, *Principles of Nuclear Magnetism* (Oxford University Press, NY, 1989).

[8] G.H. Stauss, J. Chem. Phys. **40**, 1988 (1964).

[9] W.W. Warren *et al.*, Physica C **153-155**, 79 (1988).

[10] C.H. Pennington and C.P. Slichter, *Physical Properties of High Temperature Superconductors II*, D.M.Ginberg, ed. (World Scientific, NJ, 1990).

[11] D. Brinkmann, Physica C **153-155**, 75 (1988).

[12] A.J. Vega *et al.*, Phys. Rev. B **39**, 2322 (1989).

[13] W.W. Warren and R.E. Walstedt, Z. Naturforsch. **45a**, 385, (1990).

[14] C. Bucci *et al.*, Phys. Rev. B **48**, 16769 (1993).

[15] Y. Itoh *et al.*, J. Phys. Soc. Japan **61**, 1287 (1992).

[16] T. Imai *et al.*, Phys. Rev. B **47**, 9158 (1993).

[17] R.E. Walstedt and W.W. Warren, Science **248**, 1082 (1990).

[18] J. Mustre de Leon *et al.*, Phys. Rev. B **45**, 2447 (1992).

[19] J. Mustre de Leon *et al.*, Phys. Rev. Lett. **68**, 3236 (1990).

[20] S.D. Conradson *et al.*, Science **248**, 1394 (1990).

[21] M. Weller, Mat. Science Forum **119-121**, 667, (1993).

[22] D.N. Lee and B. Lee, J. Am. Ceram. Soc. **76**, 1609 (1993).

[23] J.R. LaGraff and A. Payne, Physica C **212**, 470 (1993).

[24] J.R. LaGraff and A. Payne, Physica C **212**, 478 (1993).

[25] K.N. Tu *et al.*, Phys. Rev. B **39**, 304 (1989).

[26] K. Konder *et al.*, Physica C **210**, 282 (1993).

[27] S.J. Rothman *et al.*, Phys. Rev. B **44**, 2326 (1991).

[28] J.L. Routbort and S.J. Rothman, J. Appl. Phys. **76**, 5615 (1994).

[29] J.R. LaGraff and D.A. Payne, Phys. Rev. B **47**, 3380 (1993).

[30] J.R. LaGraff and D.A. Payne, Physica C **212**, 487 (1993).

[31] J.F. Baugher *et al.*, J. Mag. Res. **3**, 415 (1970).